Quaternary International 509 (2019) 87–102

Contents lists available at ScienceDirect

Quaternary International

journal homepage: www.elsevier.com/locate/quaint

Challenges in constraining ages of fluvial terraces in the Vienna Basin (Austria) using combined isochron burial and pIRIR225 luminescence dating

Sandra M. Braumann [a, *], Stephanie Neuhuber [a], Markus Fiebig [a], Joerg M. Schaefer [b], Esther Hintersberger [c], Christopher Lüthgens [a]

[a] Institute of Applied Geology, University of Natural Resources and Life Sciences (BOKU), Peter Jordan-Straße 82, 1190, Vienna, Austria
[b] Division of Geochemistry, Lamont-Doherty Earth Observatory, Columbia University, P.O. Box 1000, 61 Route 9W, Palisades, NY 10964, USA
[c] Department of Geodynamics and Sedimentology, University of Vienna, Althanstraße 14 (UZA II), 1090, Vienna, Austria

ARTICLE INFO

Article history:
Received 23 May 2017
Received in revised form
21 December 2017
Accepted 7 January 2018
Available online 1 February 2018

Keywords:
^{26}Al-^{10}Be
Terrestrial cosmogenic nuclides
pIRIR225 luminescence dating
Terrace stratigraphy
Middle Pleistocene
Danube terrace

ABSTRACT

Burial dating with terrestrial cosmogenic nuclides and luminescence dating techniques have become two powerful tools to temporally constrain Quaternary deposits. A combination of both methods at the same geological setting has rarely been realized to date, although their viable time frames overlap by several tens of thousands of years. When Middle Pleistocene sediments with depositional ages ranging around ca. 120 ka to ca. 300 ka are targeted, both methods are employed, but come towards their lower and upper limits, respectively. A combined dating approach can be worthwhile at this age range and allows not only exploring the edges of both methods, but holds the opportunity to do a cross-check of results at an age spectrum, where both dating techniques are at risk to become fuzzy.

Here we present a case study where numerical ages of two Middle Pleistocene terraces located in the Vienna Basin were generated by combining burial and luminescence dating. A variety of processes, such as changing sediment input rates, erosion, and tectonics controlled the formation of fluvial terraces in the basin and shaped its complex modern surface. Age correlation of the evolved mosaic of blocks and dislocated sediment bodies is challenging and requires quantitative geochronological information in order to establish a coherent terrace stratigraphy. Luminescence and burial samples originating from two fluvial terraces, the lower Gaenserndorf terrace (GDT) and the higher Schlosshof terrace (SHT), were analyzed and evaluated. Luminescence and burial ages at the GDT site are in good agreement and suggest a depositional age of 140 ± 170 ka bracketed by pIRIR225 luminescence ages ranging from 120 ± 10 ka to 260 ± 30 ka. Luminescence samples at the SHT site are in saturation, but provide minimum ages, which are coherent with the burial dating result of 340 ± 170 ka. The new numerical ages indicate that the vertical offset between the GDT site and the SHT site was not purely caused by fault activity, but suggest two independent episodes of sediment accumulation.

Besides providing new insights into the stratigraphic and morphological configuration of the central Vienna Basin area, the cosmogenic nuclide data set is compelling from a methodological point of view. At the GDT site, several samples exhibited ^{26}Al/^{10}Be nuclide ratios exceeding the surface production ratio of 6.75. Even though affected samples were excluded from burial age calculations, a detailed investigation on possible scenarios, which could have caused an upwards shift of ^{26}Al/^{10}Be ratios, was carried out.

1. Introduction

The Vienna Basin is located between the Eastern Alps and the West Carpathians at the border of the Czech Republic, Slovakia, and Austria. The basin is filled with marine and terrestrial sediments deposited during the Neogene and Quaternary and is crossed by the Danube river (e.g. Fink and Majdan, 1954; Küpper, 1955; Fuchs and

* Corresponding author.
E-mail addresses: sandra.braumann@boku.ac.at (S.M. Braumann), stephanie.neuhuber@boku.ac.at (S. Neuhuber), markus.fiebig@boku.ac.at (M. Fiebig), schaefer@ldeo.columbia.edu (J.M. Schaefer), esther.hintersberger@univie.ac.at (E. Hintersberger), christopher.luethgens@boku.ac.at (C. Lüthgens).

https://doi.org/10.1016/j.quaint.2018.01.009

Grill, 1984; Decker et al., 2005; Hölzel et al., 2010). During the Pleistocene, climatic cooling caused the abrasion and subsequent transport of glacial debris from inneralpine areas to the foreland providing sediment to form large gravel terraces along the Danube and its tributaries (van Husen and Reitner, 2011). A combination of climate oscillations and over-regional tectonic uplift provided ideal conditions to the formation of a complex terrace staircase in the basin (Royden, 1985; Peresson and Decker, 1997; Salcher and Wagreich, 2010). Multiple Pleistocene terrace levels were identified along the southern riverbank of the Danube showing pronounced differences in altitude. Interestingly, an equivalent of this staircase is not mirrored as prominently north of the Danube. While to date, seven Pleistocene stratigraphic units are documented in the southern part (e.g. Fink and Majdan, 1954; Lüthgens et al., 2017 and references therein), only three terrace units have been found in the area to the north: the Gaenserndorf terrace (GDT), the Schlosshof (SHT) and the terrace west of Seyring (TWS) (Fig. 1). An extensive Miocene fault system underlying the sediments was reactivated during the Pleistocene. It was influencing the morphology of the terraces and caused vertical displacement of individual fragments (Decker et al., 2005; Wessely, 2006).

The traditional approach of correlating fluvial terraces is based on geomorphological configurations, in particular base level elevation (Penck and Brückner, 1909). Connected base levels are interpreted towards the same period of accumulation. In an area with evidence of an interplay of multiple processes, e.g. tectonic uplift, sediment input and sediment preservation, cryoturbation and local dislocation, this approach might result in misleading correlations. In the Vienna Basin, vertical and lateral displacement of individual terrace segments notably complicates terrace correlation based on comparing base levels. Numerical ages of individual sediment bodies are therefore vital to establish a coherent terrace stratigraphy and to improve the temporal and spatial understanding of surface changes during the Quaternary.

Age information is sparse in the basin area and limited to only a few data sets: (1) dendrochronology and radiocarbon dates gained from the analysis of reworked wood fragments, which were found embedded in the lowermost terrace level and are associated with the Holocene (Fink, 1977, 1981); (2) luminescence ages and burial ages from a core drilled south of the Danube, where luminescence data (based on the measurement of the post infrared, infrared stimulated luminescence signal at 225 °C (pIRIR225) of potassium-rich feldspar) provide minimum ages ranging around 250 ka for the upper section of the core (signals are in field saturation), and where isochron burial dating yields a Late Pliocene age for cobbles collected from deeper sections of the core (Lüthgens et al., 2017); and (3) Optically Stimulated Luminescence (OSL) ages from the GDT setting (Weissl et al., 2017), which include reliable ages from MIS 2. These were determined by combined measurement of luminescence signals of both quartz and potassium-rich feldspar. However, older ages only rely on measurements of potassium-rich feldspar using the IR signal stimulated at 50 °C (IR50). This signal is known to be prone to fading, an athermal signal loss over time (Wintle, 1973), leading to age underestimation if not corrected for. Because of the high dose range of the samples, the authors decided not to apply any fading correction. In addition, the luminescence signals for the respective samples approach field saturation. Taking these factors into account, ages from Weissl et al. (2017), for which no age control from quartz measurements is available (especially around and above 200 ka), must be interpreted as minimum ages.

Here, we present a new geochronological case study targeting terrace bodies in the Vienna Basin, where two independent physical dating methods were applied to put time constraints on the deposition of the GDT and the SHT north of the Danube: isochron burial dating using the cosmogenic isotope pair ^{26}Al and ^{10}Be and pIRIR225 luminescence dating.

The objectives of this study are:

(1) to test the feasibility of burial dating at the central Vienna Basin area north to the Danube, in particular targeting the lower GDT, in order to assess whether the level of cosmogenic nuclide concentrations in these sediments is high enough to be analyzed with Accelerator Mass Spectrometry (AMS).
(2) to realize a cross-check on burial and luminescence (pIRIR225) ages, as both dating methods are frequently used

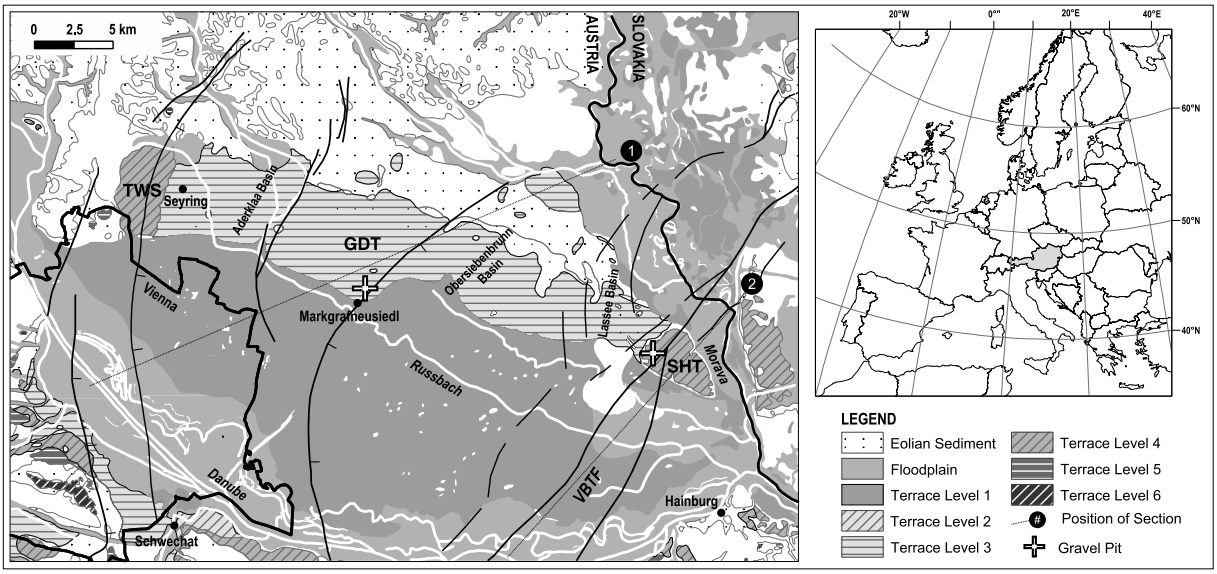

Fig. 1. Map displaying the northern and part of the southern terrace staircase along the Danube in the central Vienna Basin area, the Gaenserndorf terrace (GDT), the Schlosshof terrace (SHT) and the terrace West of Seyring (TWS). Crosses indicate outcrops which were sampled for cosmogenic nuclide and luminescence analysis. The solid thick line towards the East specifies the Austrian-Slovakian border, while the solid thick line towards the West circles the city area of Vienna. Thin black lines are active faults dissecting the Miocene base of the Vienna Basin, e.g. VBTF (Vienna Basin Tranform Fault). Dashed thin lines mark the location of transects illustrated in Fig. 2.

to answer geochronological questions related to Quaternary stratigraphy. Time frames covered by luminescence dating range from a few tens of years to several hundreds of thousands of years (Wintle, 2008). Burial dating spans ca. 100 ka to 5 Ma (Granger and Muzikar, 2001), thus overlapping with the luminescence method. The GDT and the SHT, which are estimated to have formed during the Middle Pleistocene (Küpper, 1955; Fink and Majdan, 1954; Thenius, 1974), are suited to test luminescence and burial dating independently.

(3) to generate novel and robust geochronological information at the Vienna Basin area, which allows constraining the age of two Middle Pleistocene terraces (GDT and SHT).

(4) to scrutinize a cluster of elevated $^{26}Al/^{10}Be$ ratios, which occurred among some of the samples collected from the GDT and to make an attempt to explain these irregularities.

2. Geological setting

The Vienna Basin is a subsiding pull-apart structure with dimensions of 200 km in length, 55 km in width and up to 5.6 km in depth. The Neogene to Quaternary infill mainly consists of fine sediments and gravel deposits (e.g. Fink and Majdan, 1954; Royden, 1985; Kováč et al., 2004). The basin's subsidence started approximately 17 Ma ago, during the Early Miocene. The structure formed following an extensive NE-SW trending Miocene fault system with the most prominent lateral (sinistral) displacement along the Vienna Basin Transform Fault (VBTF) at its SE margin (Decker, 1996, Fig. 1). Basin inversion and only scarce presence of Pliocene sediments indicate that subsidence halted during the Late Miocene. Evidence of sediments attributed to the Miocene and found at elevations of up to 440 m asl at the basin's margin, together with the fact that a terrace staircase developed during the Quaternary, point to a major uplift from Late Pannonian times onward (Decker, 1996; Salcher, 2008).

During the Quaternary, the fault system was active and has had an impact on the continuity of the sediment record, in particular at the central part of the basin. In the study area, normal faults connected to the Neogene fault system below the investigated terraces, are very likely to have caused a vertical displacement of individual segments (Decker et al., 2005; Hinsch et al., 2005; Salcher and Wagreich, 2010; Hinsch and Decker, 2011 and references therein). Several geomorphological indicators stress the tectonic control of some (NE-SW trending) fault scarps that border the terraces, while other scarps evolved from erosion by the Danube river and local tributaries (Beidinger and Decker, 2011; Decker et al., 2005; Weissl et al., 2017).

The syntectonic filling of the basin with largely marine sediments began approximately 17 Ma ago during the Badenian, and continued up to Late Pannonian times, ca. 8 to 9 Ma ago (Kováč et al., 2004; Strauss et al., 2006; Beidinger and Decker, 2011). This period was followed by a hiatus of sediment deposition during the Pliocene until the beginning of the Quaternary, when fluvial, lacustrine and eolian deposits resumed to accumulate at local depocenters (Beidinger and Decker, 2014; Decker et al., 2005; Hinsch et al., 2005; Salcher et al., 2012; Salcher et al., 2017). While Neogene basin fillings amount to thicknesses of up to 5.6 km, Quaternary sediments reach only thicknesses of up to 170 m (Kullmann, 1966; Salcher, 2008; Beidinger and Decker, 2014; Lee and Wagreich, 2016). This relatively thin and young sediment cover largely consists of gravel and sand layers mainly delivered by the Danube and Morava, but also by some smaller rivers such as the Russbach (Fig. 1). Most debris from inneralpine regions and the Bohemian Massif passed through the basin and was ultimately deposited farther to the East (e.g. Ruszkiczay-Rüdiger et al., 2016; Tanasković et al., 2017). A small fraction, however, was preserved in the Vienna Basin and formed terraces. A correlation of these terrace sediments by field geologic methods is difficult, not only due to a plurality of processes, which affected the basin during the Quaternary, but also because of their uniform quartz rich lithology and a paucity of fossils, which are limited to the loess cover partly blanketing the terraces.

2.1. GDT setting

The Holocene flow path of the Danube delimits the southern margin of the GDT (Fig. 1, terrace level 1). Westwards, the terrace adjoins the TWS, which rests upon Penninic Units. Its base is located ca. 4–6 m above the base of modern Danube sediments (Fig. 2a). The GDT is dissected by a number of normal faults that have presumably controlled the formation of small subbasins inside the Vienna Basin (Aderklaa, Obersiebenbrunn and Lassee basin; Decker et al., 2005, Fig. 1). Towards the East, the Lassee basin separates the GDT from the SHT (Beidinger and Decker, 2011). The GDT sediment largely consists of coarse clast-supported gravel with coarse to medium sandy matrix and subordinate sand lenses that are cut by overlying gravel beds. The total thickness of the terrace deposit lies between 10 and 15 m. Often, the uppermost 3–4 m are affected by intense cryoturbation and may be covered by loess of varying thicknesses. Clasts are mostly well-rounded, typical for fluvial transport.

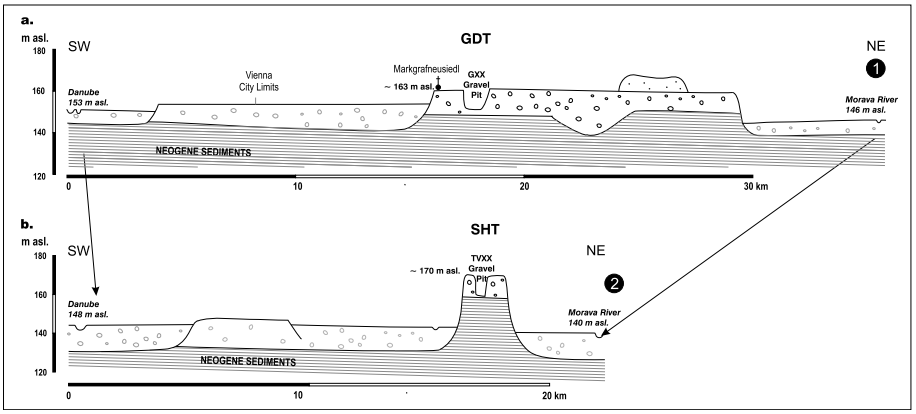

Fig. 2. NE-SW transects cutting through (a.) Gaenserndorf terrace (GDT) and (b.) Schlosshof terrace (SHT). Map view positions of the transects are provided in Fig. 1. The GDT's base level lies at a lower elevation (ca. 150 m asl) compared to the SHT's (ca. 160 m asl), which is also reflected in the terraces' deviating surface elevation.

The sampled outcrop is located in an abandoned gravel pit (E 16.6329444, N 48.2927778°, altitude 163 m asl) and consists of intermittent sand lenses and gravel bed units forming a typical braided river facies, which is classified as high-energy deposit. The clast-supported matrix in the sampled sediment layer provides an abundancy of cobbles suited for cosmogenic nuclide analysis. Ten samples were collected from a sediment layer at ca. 4.5 m depth, five cobbles at position GXX-II and five more clasts at position GXX-III (Fig. 3). Four luminescence samples, MAR-01 to MAR-04, were collected from sand layers throughout the profile at varying depths (Fig. 4).

Cosmogenic nuclide sample position GXX-II is located at the lee side of a weathered granite boulder. The presence of the boulder suggests that all pebbles were washed into their recent position in the course of a single phase of sedimentation and is assumed to reduce the probability of postdepositional movement. Isolated gneiss or granite boulders are a frequent phenomenon in sand and gravel terraces at the study area (Eppensteiner et al., 1973). This type of boulder found in a facies dominated by smaller grain sizes is explained by ice rafting or root transport. On top of the block, a small channel structure, typical for braided river systems, was identified. The fossil channel showed foresets with intermittent cobble beds. The sampled layer's limitation towards the top unit was horizontal. The stratification showed no evidence of vertical mixing or tectonic impact. Pronounced manganese and iron oxide horizons marked changing paleo-water conditions in depths of 3–3.5 m below surface, as well as in the sampled sediment layer.

2.2. SHT setting

The SHT is roughly triangularly shaped, bordered by the Lassee fault system to the West (Beidinger and Decker, 2011) and delimited by fluvial erosion by the rivers Danube and Morava to the South and East (Fig. 1). The base of the terrace lies ca. 25–30 m above the modern Danube sediments' base level and is significantly higher compared to the GDT elevation (Fig. 2b). The sampling sites for cosmogenic nuclide dating and luminescence dating are located in an active gravel pit with predominantly gravel sized unconsolidated fluvial sediments and subordinate sand lenses (Fig. 5). The top of all sediments is influenced by cryoturbation down to about 3.5 m. The quarry's base is formed by Neogene clays that are covered with mainly coarse-grained fluvial gravels and sands. Sediments are affected by a side branch of the Lassee flower structure (Beidinger and Decker, 2011) that offsets both, the Neogene and the Quaternary. The clays at the eastern side are displaced from ca. 153 m asl to 164 m asl.

The five clasts sampled for cosmogenic isotope burial age dating (E 16.8874056°, N 48.2388361°, altitude 153 m asl) are located ca. 3 m above the Neogene base and 10 m below the old surface from the western (basinward) side of the fault. The six luminescence samples originate from both sides of the fault (Fig. 5).

3. Methods

3.1. Isochron burial dating with cosmogenic nuclides

3.1.1. Principle of isochron burial dating

When secondary cosmic rays, comprising neutrons and muons, reach the earth's surface, they interact with the upper layers of the lithosphere and cause the in situ production of stable and unstable terrestrial cosmogenic nuclides (Lal and Arnold, 1985; Lal, 1988; Nishiizumi et al., 1986; Gosse and Phillips, 2001). The dating of buried sediments using these nuclides relies on their time-dependent, differential decay in the subsurface, where samples are largely shielded from cosmic radiation (Nishiizumi et al., 1986; Klein et al., 1986). Burial dating requires the analysis of at least two

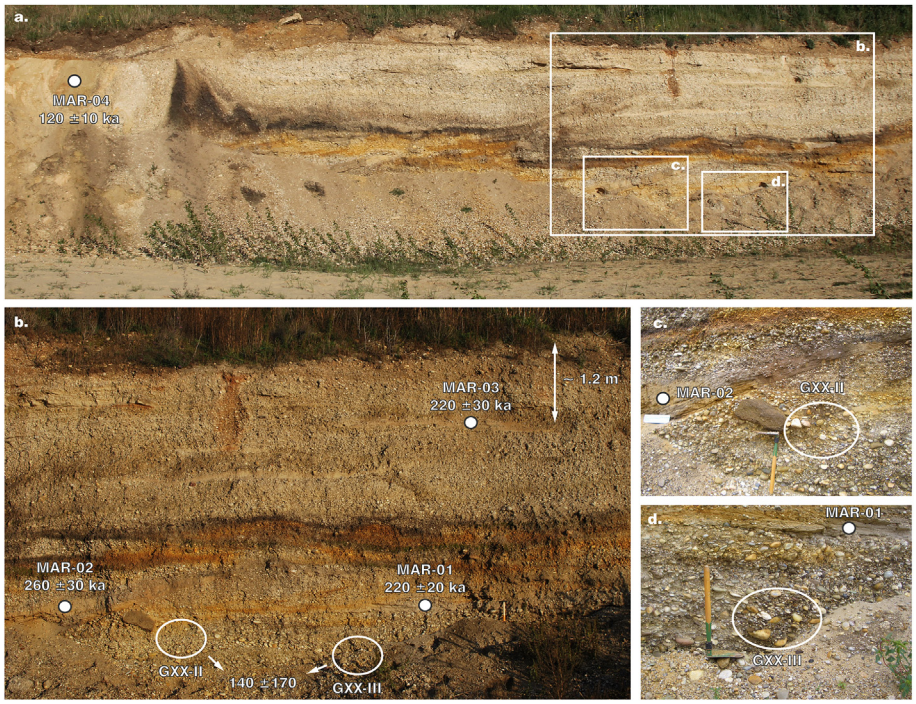

Fig. 3. (a.) Outcrop Gaenserndorf terrace (GDT). Luminescence sample MAR-04 was collected from a surface-near sand lense further southwards to the cosmogenic nuclide samples (GXX-II and GXX-III). Positions of the remaining luminescence samples (MAR-01 to MAR-03) are shown in (b.),(c.) and (d.) together with cosmogenic nuclide sample positions. (c.) Zoom on cosmogenic nuclide sample set position (GXX-II) at the lee side of a crystalline block and luminescence sample MAR-02. (d.) Zoom on cosmogenic nuclide sample set position (GXX-III) and luminescence sample MAR-01.

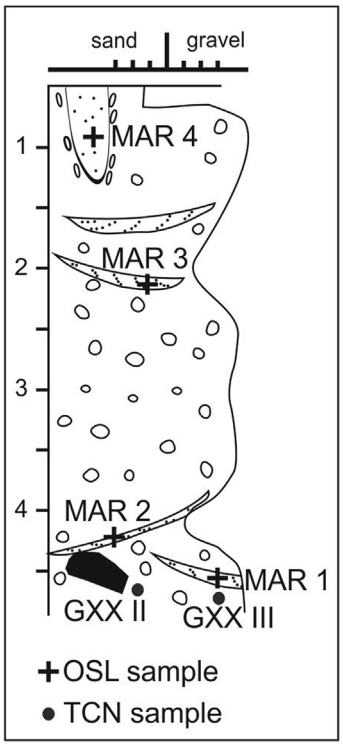

Fig. 4. Profile GDT outcrop; luminescence (OSL) sample positions are marked with a cross, cosmogenic nuclide sample positions are indicated with a circle.

nuclides, as there are two unknowns in the sample's history: first, the time of exposure and second, the time of burial itself (Nishiizumi et al., 1986; Granger and Muzikar, 2001; Granger, 2006). ^{26}Al and ^{10}Be are a favored pair to be combined for burial dating: (1) Both nuclides are produced in quartz, which is ubiquitous and highly resistant to weathering, (2) ^{26}Al and ^{10}Be show similar geochemical behavior, which eases sample preparation, (3) their surface production rates are linear proportional at the range of regular attenuation lengths (Brown et al., 1992; Gosse and Phillips, 2001; Argento et al., 2013) and (4) the isotopes half-lives deviate by a factor of two (^{10}Be $\tau_{1/2} = 1.387 \pm 0.012$ Ma and ^{26}Al $\tau_{1/2} = 0.705 \pm 0.024$ Ma; Chmeleff et al., 2010; Korschinek et al., 2010; Nishiizumi, 2004).

^{26}Al and ^{10}Be are built up at well-constrained production rates at the earth's surface. While local production rates vary depending on altitude, geomagnetic latitude and shielding (Nishiizumi et al., 1989; Stone, 2000), the nuclides' surface production ratio is assumed to be stable at a value of ca. 6.75, regardless of the sample's geographic location (Nishiizumi et al., 1989; Kubik et al., 1998; Balco and Rovey, 2008). When terrestrial rock is covered and therefore less affected by cosmic ray bombardment, nuclides begin to disintegrate, ^{26}Al approximately twice as fast as ^{10}Be. The decay process leads to a gradual drop of the ^{26}Al/^{10}Be ratio, providing key information with respect to the sample's burial time. Nuclide ratios measured in buried samples and related to the initial surface production ratio via the law of decay allow the calculation of burial ages.

At the Vienna Basin settings, where it is aimed to put age constraints on abandoned fluvial terraces, one important factor complicates this simple burial model: postburial production by muons. Approximately 98% of the ^{26}Al and ^{10}Be inventory in terrestrial material at the surface accumulate due to spallogenic production by neutrons. However, this production pathway is limited to the earth's surface and the very upper centimeters of soil or rock. The remaining 2% are produced by muons, short-lived energetic lepton particles, which show much weaker interaction with matter than neutrons (Braucher et al., 2003; Brown et al., 1995; Lal, 1988). Muons have physical properties that allow the particles to travel into greater depths of the lithosphere, where they cause nuclide production. Through this production pathway, ^{26}Al and ^{10}Be is added to the nuclide inventory subsequent to the sample's burial, a process that needs to be taken into account when dating sediment layers with incomplete shielding.

Given the depth profile of muon attenuation, postburial nuclide production is most effective at shallow depths, where spallogenic production becomes negligible (>3 m), and muonic impact is still strong enough to penetrate terrestrial material (<30 m) (Granger and Muzikar, 2001; Dunai, 2010; Braucher et al., 2013). Fluvial terraces fall into this category, so that postburial production needs to be addressed.

Balco and Rovey (2008) put forward the idea to broaden the field of isochron applications to geochronological questions in sedimentary deposits that are potentially affected by postburial production. The strategy is to accomplish correction for muon production by treating clasts, which share their final burial episode, as an amalgamated sample. Clasts that were presumably deposited in the course of the same sedimentary event and are collected from the same stratigraphic layer have been exposed to an identical rate of postburial production from their deposition onward. Predepositional erosion and transport are very likely to vary among individual samples, therefore causing scatter in nuclide concentrations. Nevertheless, muon production subsequent to burial is constant for all clasts. When this assumption is valid, nuclide concentrations of clasts sampled from the same depth, show a linear trend in a diagram, where ^{26}Al is plotted against ^{10}Be. The slope of the isochron derived from the sample set by regression depends on the amalgamated sample's collective age of deposition, on the ^{26}Al/^{10}Be production ratio and on the nuclides' decay constants, but is insensitive to postburial production. Outliers, for example reworked clasts with a different burial history, are easy to identify as they do not plot along the isochron.

The concept of isochron burial dating using cosmogenic nuclides was first applied by Erlanger et al. (2012), who put time constraints on fluvial terraces in South Africa. Since then, the method has become more and more popular for settings, where postburial production is likely to contribute to the sediments' nuclide inventory, i.e. sediments at shallow depths (e.g. Balco et al., 2013; Çiner et al., 2015; Matmon et al., 2015; Granger et al., 2015; Bender et al., 2016; Schaller et al., 2016; Zhao et al., 2016; Akçar et al., 2017; Tu et al., 2017).

3.1.2. Sample preparation and sample analysis

Nuclide extraction of all, in total ten, GDT samples, was accomplished at the cosmogenic isotope laboratory at the Lamont-Doherty Earth Observatory, according to the laboratory's protocol (LDEO, 2009a; LDEO, 2009b). ^{10}Be/^{9}Be and ^{26}Al/^{27}Al ratios were measured at the Center for Accelerator Mass Spectrometry at the Lawrence Livermore National Laboratory (LLNL) using the standards 07KNSTD3110 (Be) and KNSTD30960 (Al), respectively.

The five SHT clasts were processed following the procedure of Granger et al. (2015) at the Geochronology Laboratory of the Department of Lithospheric Research (University of Vienna), and at the Laboratory for Cosmogenic Nuclide Extraction at the Institute of Applied Geology (BOKU Vienna). Aluminum and Beryllium oxides were analyzed at PRIME laboratory and VERA, respectively. Standards at PRIME are characterized by Nishiizumi (2004) for Aluminum and by Nishiizumi et al. (2007) for Beryllium. Standards

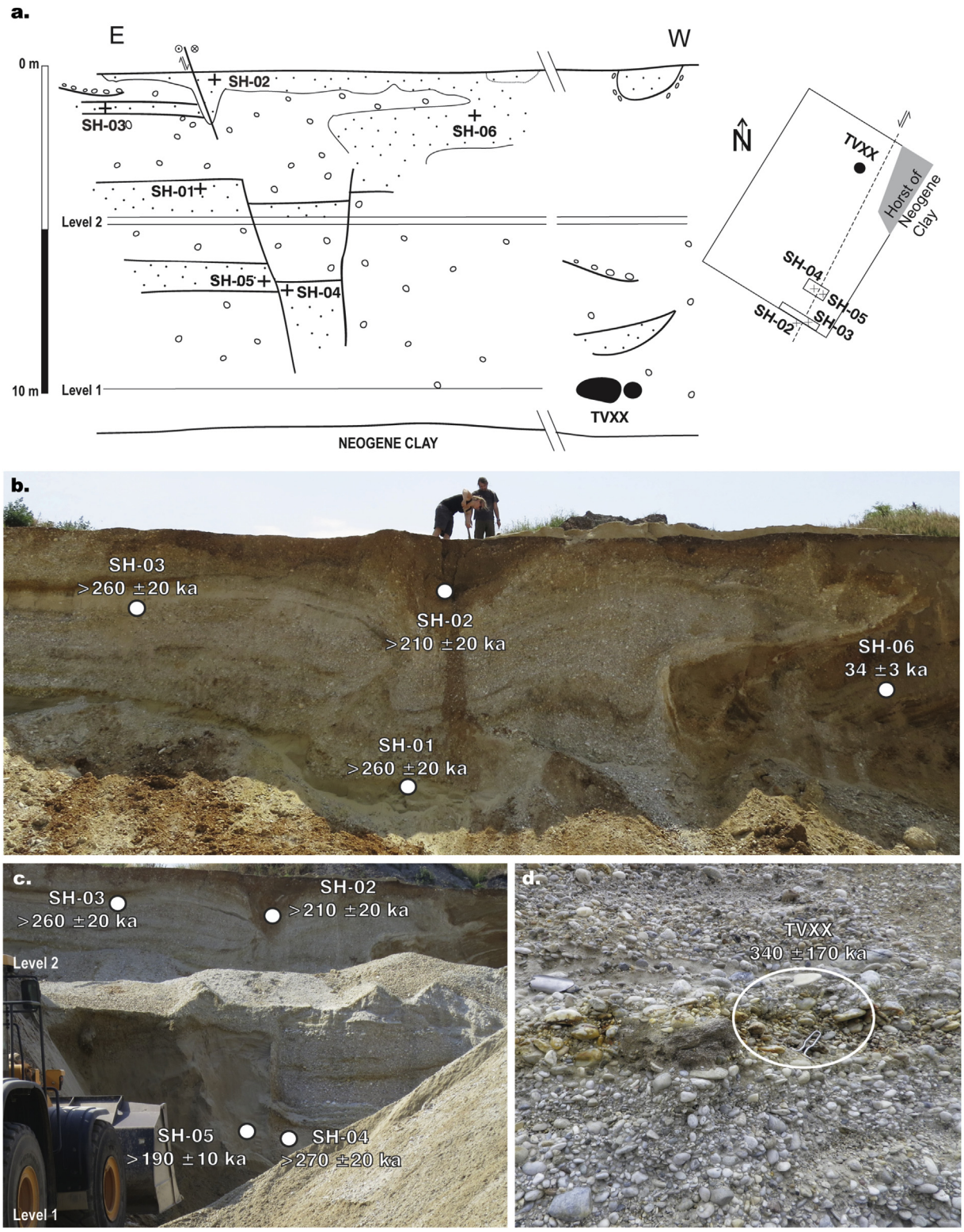

Fig. 5. Outcrop Schlosshof terrace (SHT). (a.) Transect displays position of luminescence samples (SH-01 to SH-06) and location of cosmogenic nuclie sample set (TVXX). Map view displays position of strike slip fault; note that the cosmogenic nuclide sample set and SH-04 are both located at the faults hanging wall. (b.) Sample position SH-01 to SH-03, and SH-06 at level 2. The section is extremely cryoturbated in the upper 3.5 m above the fault. (c.) Sample positions SH-02 to SH-05 at level 1. (d.) Cosmogenic nuclide sample set TVXX.

at VERA are secondary standards. For Aluminum measurements, two standards were used: AW-V-2 with an $^{26}Al/^{27}Al$ ratio of 2.71 ± 0.02^{-12} and AW-V-3 with a ratio of 3.55 ± 0.05^{-12}. For Beryllium, the secondary standard is calibrated to NIST 4325 with a $^{10}Be/^{9}Be$ ratio of 1.704 ± 0.03^{-12}.

Elemental analysis to quantify total Aluminum in samples was

performed using ICP-OES. Total uncertainties on ^{10}Be and ^{26}Al concentrations are calculated combining the AMS measurement error, uncertainties on the nuclides' surface production rates, uncertainties on the nuclides half-lives and ICP-OES errors in the case of Aluminum.

3.1.3. Isochron age calculations

Burial ages were computed following Granger (2014) using the corresponding MATLAB script. The initial nuclide ratio (R_{init}) was set at 6.75. As ^{10}Be reference production rate at Sea Level High Latitude (SLHL), 4.00 ± 0.32 atoms/g qtz and yr was adopted (Borchers et al., 2016). In order to normalize nuclide concentrations, the local ^{10}Be production rate was estimated using the scaling scheme of Stone (2000). Normalized ^{26}Al measurements were first plotted against normalized ^{10}Be measurements and a regression line was fitted to the data using the routine described by York (York et al., 2004). From the slope of this line, an initial burial age was calculated (t_{bur}). Nuclide contribution due to postburial production is indicated by the intercept of the regression line resulting from the first isochron estimate, and a line generated by modeling postburial production of ^{26}Al and ^{10}Be under the assumption of steady erosion in the source area (Erlanger et al., 2012; Granger, 2014; Zhao et al., 2016, Akçar et al., 2017). The resulting postburial production component was then subtracted from measured nuclide concentrations, allowing to isolate the inherited nuclide component ($N_{Be,inh}$) at $t = t_{bur}$. In order to calculate $N_{Be,inh}$ at $t_{bur} = 0$, a ^{10}Be linearization factor is introduced to correct all ^{10}Be measurements for nuclide production subsequent to the samples' burial. Normalized ^{26}Al concentrations were then plotted against linearized ^{10}Be concentrations with the postburial production component added. The slope of the resulting isochron allowed estimating a new burial age. The quantification and correction for postburial production was iterated until ages converged. In order to calculate age uncertainties, a Monte-Carlo simulation based on the recursive fits of ^{26}Al and ^{10}Be data was performed and probability histograms were generated. The simulation was repeated 10,000 times by randomly varying ^{26}Al/^{10}Be ratios within the measured errors bars. Resulting ages are the respective mean ages with 1σ standard deviation derived from the histograms.

3.2. Luminescence dating

3.2.1. Principle of luminescence dating

OSL dating techniques enable the determination of depositional ages of sediments. During sediment transport, the light sensitive luminescence signal stored in quartz and potassium-rich feldspar minerals is erased (zeroed or optically bleached). After deposition of the sediments, naturally occurring ionising radiation induces a new build-up of charge stored within defects of the crystal lattice of minerals, which function as natural dosimeters. Once the rate of this build-up of charge (termed the doserate) and the energy stored within the crystals (termed the equivalent dose) is known, a depositional age can be calculated using the general luminesce age equation age *(a) = equivalent dose (Gy)/doserate (Gy/a)*. For further details concerning luminescence dating techniques in general, we refer to a number of overview papers: Preusser et al. (2008), Rhodes (2011), and Wintle (2008).

In this study, only potassium-rich feldspar was used as a dosimeter, because of the expected age range from previous work (Weissl et al., 2017), which implied equivalent doses clearly beyond the signal saturation level of quartz for the sediments under investigation. This assumption was confirmed by test measurements on the stratigraphically youngest sample from the GDT site, which clearly showed the quartz signal to be in field saturation. Therefore, potassium-rich feldspar was used for all analyses in this study. Whenever K-feldspar is used for luminescence dating, it has to be taken into account that an athermal signal loss over time (termed anomalous fading) frequently occurs (Wintle, 1973), resulting in potential age underestimation if not detected and corrected for. However, the applicability of fading correction models (e.g. Huntley and Lamothe, 2001) in high dose ranges, as expected in this study, is rather limited. Thus, we chose to apply a measurement protocol reducing the expected amount of fading compared to the classical infrared stimulated luminescence signal of feldspar measured at a temperature of 50 °C (IR50) by measuring a post infrared, infrared stimulated signal (pIRIR) at an elevated temperature (Buylaert et al., 2009, 2012). Such pIRIR signals were proven to show significantly less or even negligible fading compared to the IR50 signal, ideally making it possible to circumvent fading correction completely.

3.2.2. Sampling and sample preparation

Samples were collected from suitable sand layers and sand lenses from both locations under study (Figs. 3 and 5) by driving opaque stainless steel cylinders into the freshly cleaned sediment surface. Additional samples from the direct surroundings of the luminescence samples were taken for determination of the radionuclide content. All sample preparation was conducted at the Vienna Laboratory for Luminescence dating (VLL) under subdued red light conditions. The sampling cylinders were opened and the outer few centimetres of material were removed because of light exposition during the sampling process. Separates of potassium-rich feldspar were prepared according to standard procedures (described in detail in Lüthgens et al., 2017; Rades et al. in press) by drying, sieving, chemical treatment (10% HCl to remove carbonates, 10% H_2O_2 to remove organics, and sodium-oxalate for dispersion of particles), and density separation (using LST FastFloat). Samples for radionuclide determination were first dried, and subsequently stored in sealed Marinelli beakers (500 ml, containing about 1 kg of sample material) for at least four weeks for establishing secondary secular radon equilibrium.

3.2.3. Experimental setup

All measurements for the determination of the equivalent dose were conducted at the VLL using two RISØ TL-OSL DA-20 luminescence reader systems (Bøtter-Jensen et al., 2000, 2003), each equipped with a ^{90}Sr/^{90}Y beta source delivering a doserate of approximately 0.1 Gy/s. The emission from multigrain feldspar aliquots with a sample diameter of 1 mm (each containing about 20–30 grains of grain size fractions 200–250 μm or 200–300 μm, respectively) was stimulated using infrared (IR, 875 nm) LEDs and detected through a LOT/Oriel D410/30 optical interference filter, selecting the K-feldspar emission at 410 nm (Krbetschek et al., 1997). A range of pre-tests was conducted for a selected number of samples in order to prove the suitability of the chosen pIRIR measurement protocol using a stimulation temperature of 225 °C, and a preheat temperature of 250 °C held for 60 s. Results from dose recovery experiments showed excellent performance for both evaluated signals, the IR50 signal taken from the pIRIR measurements, and the pIRIR225 signal (Table 1). Signals were integrated over the first second of stimulation with the last 10 s subtracted as background. Based on the results from dose recovery experiments the following rejection criteria were defined: recycling ratio <5%, recuperation <5% of the natural signal, test dose error <5%, and signal >3σ above background. Fading tests were conducted for two samples following the approach of Auclair et al. (2003), but modified to also detect the pIRIR225 signal. Results from these tests exhibit g-values of about 3% per decade for the IR50 signal, and g-values around 1% per decade for the pIRIR225 signal, therefore showing similar values as samples from previous work conducted

Table 1
Results from luminescence pre-tests.

Sample ID Lab	Sample ID Field	Dose Recovery Test [n]	Recovery Ratio IR50 [a] [−]	Recovery Ratio pIRIR225 [a] [−]	Fading Test [n]	g-value IR50 [b] [%]	g-value pIRIR225 [b] [%]	Residuals [c] [n]	Residual IR50 [a] [Gy]	Residual pIRIR225 [a] [Gy]
VLL-0199-L	MAR-01	4	1.1 ± 0.1	1.1 ± 0.1	6	3.0 ± 0.3	1.1 ± 0.2	3	1.9 ± 0.5	12.2 ± 2.8
VLL-0201-L	MAR-03	4	0.9 ± 0.1	1.1 ± 0.1	n/a	n/a	n/a	n/a	n/a	n/a
VLL-0210-L	MAR-04	n/a	n/a	n/a	6	3.3 ± 0.4	1.3 ± 0.2	3	1.4 ± 0.1	13.7 ± 1.9
VLL-0234-L	SH-06	4	1.0 ± 0.1	1.0 ± 0.1	n/a	n/a	n/a	n/a	n/a	n/a

[a] Average ± standard deviation.
[b] Weighted mean ± standard error.
[c] Exposed on the laboratory windowsill for ca. 3 days, Vienna, summer of 2015.

in the Vienna Basin (Lüthgens et al., 2017). This also holds true for the relatively low residual signals detected in this study (ca. 1–2 Gy for the IR50 signal, and ca. 12–14 Gy for the pIRIR225 signal, see Table 1).

The content of naturally occurring radionuclides (^{238}U and ^{232}Th day chains, as well as ^{40}K) contributing to the doserate of the samples was determined at the VLL by high resolution, low-level gamma spectrometry using a Canberra HPGe (40% n-type) detector. Samples were measured for 24 h to achieve a preferable signal to noise ratio.

For the calculation of the overall doserate, the external doserate was calculated based on the results from the gamma spectrometry measurements using conversion factors of Adamiec and Aitken (1998) and β-attenuation factors of Mejdahl (1979), as well as an average alpha efficiency (a-value) of 0.08 ± 0.02. For the time of burial, we assume an average estimated water content of 15 ± 5% for all samples, with the assigned uncertainty effectively covering relatively dry to almost saturated conditions. For the calculation of the internal doserate, an average potassium content of 12 ± 0.5% (following Huntley and Baril, 1997) was taken into account. Finally, the cosmic doserate was determined according to Prescott and Stephan (1982) and Prescott and Hutton (1994), based on the geographical position of the sampling spot (longitude, latitude, and altitude), the depth below surface, as well as the average density of the sediment overburden. To adequately reflect uncertainties of these values, the cosmic doserate was assigned with an error of ±10%.

4. Results

4.1. Isochron burial ages

^{10}Be/^{9}Be and ^{26}Al/^{27}Al ratios of both, the GDT and the SHT, are reported in Tables 2 and 3. Resulting ^{26}Al/^{10}Be ratios are listed in Table 4. Four GDT samples showed an unusual pattern of elevated ^{26}Al/^{10}Be nuclide ratios, far above the ^{26}Al/^{10}Be ratio of 6.75, and were thus plotting in the "forbidden zone" above the surface exposure line of the isochron plot (Fig. 6a) (Lal, 1991). This pattern, occurring at the GDT setting only, might be explained by the presence of two separate clast populations, one which originates from slowly to moderately eroding surfaces and areas with small hillslope gradients (possibly from a source in the Bohemian Massif) or from re-deposited older gravel, and a second population originating from fast eroding surfaces, presumably the Alps. The latter (supposedly glacially impacted) set of samples with ^{26}Al/^{10}Be ratios exceeding 6.75 is prone to have an initial nuclide ratio higher than

Table 2
Analytical Be data. GDT samples (IDs GXX) were processed at LDEO and measured at LLNL, normalized to standard 07KNSTD3110 = 2.85×10^{-12}. Three procedural blanks were processed along with both batches and showed ratios from 1.787×10^{-16} to 2.323×10^{-16}. GXX-II-1 was included in both batches for quality control. The two subsamples were measured in the course of two separate AMS runs. GXX-II-1 (1) and GXX-II-1 (2) are deviating by 2.23%. This value lies below the AMS measurement uncertainty of both subsamples. SHT samples (IDs TVXX) were processed at the Vienna Laboratory (VL) and were measured at VERA and PRIME lab, respectively. Standards used at PRIME lab were characterized by Nishiizumi (2004). At VERA, the secondary Be standard is calibrated to NIST 4325 with a ^{10}Be/^{9}Be ratio of 1.704 ± 0.03^{-12}. Be concentrations of double measurements were averaged for burial age calculations.

Site	Sample ID	TCN LAB/AMS	Quartz [g]	^{9}Be carrier [mg]	^{10}Be/^{9}Be [−]	Error ratio AMS [%]	^{10}Be [atoms/g qtz]	Total error ^{10}Be [%]
GDT	GXX-II-1 (1)	LDEO/LLNL	24.9980	0.1820	5.405E-14	3.83	26298	6.29
	GXX-II-1 (2)	LDEO/LLNL	24.9272	0.1769	5.673E-14	2.31	26906	5.50
	GXX-II-2	LDEO/LLNL	25.2633	0.1782	9.213E-14	1.90	43428	5.34
	GXX-II-3	LDEO/LLNL	25.3911	0.1793	6.220E-14	2.63	29352	5.64
	GXX-II-5	LDEO/LLNL	25.3505	0.1785	6.338E-14	2.35	29821	5.51
	GXX-II-10	LDEO/LLNL	24.7806	0.1764	3.362E-13	1.88	159934	5.33
	GXX-III-1	LDEO/LLNL	24.3382	0.1763	9.097E-14	1.90	44038	5.34
	GXX-III-2	LDEO/LLNL	25.0836	0.1819	1.185E-13	2.08	57443	5.40
	GXX-III-3	LDEO/LLNL	24.8726	0.1823	6.332E-14	2.33	31015	5.50
	GXX-III-4	LDEO/LLNL	25.0268	0.1823	5.827E-14	2.19	28365	5.45
	GXX-III-5	LDEO/LLNL	25.2166	0.1828	9.372E-14	2.04	45400	5.39
SHT	TVXX 1	VL/VERA	44.1634	0.2477	1.150E-13	6.96	43103	8.79
	TVXX 2	VL/VERA	40.5659	0.2498	7.510E-14	4.66	30901	7.11
	TVXX 4 (1.00-0.50)	VL/PRIME	32.0867	0.3616	1.168E-13	4.61	87970	7.08
	TVXX 4 (0.50-0.25)	VL/PRIME	52.4899	0.3695	1.899E-13	3.55	89333	6.44
	TVXX 5	VL/PRIME	32.7028	0.3617	3.938E-14	5.98	29107	8.03
	TVXX 6	VL/PRIME	54.0745	0.7263	5.029E-14	4.77	45138	7.19

P_{10} 4.00 ± 0.32 atoms/g yr (Borchers et al., 2016).
$t_{1/2,Be}$ 1387000 ± 12000 yrs (Korschinek et al., 2010; Chmeleff et al., 2010).
Error propagation. $Err_{total.Be} = \sqrt{err^2_{P_{10}} + err^2_{t_{1/2,10}} + err^2_{ratio}}$.

Table 3
Analytical Al data. GDT samples (IDs GXX) were processed at LDEO and measured at LLNL, normalized to standard KNSTD30960 = 3.096×10^{-11}. Two process blanks processed along with two sample batches showed ratios of 2.424×10^{-16} and 1.412×10^{-15}. GXX-II-3 provided enough material to be loaded into two AMS targets, listed as GXX-II-3 (1) and GXX-II-3 (2). Corresponding ratios deviate by 5.04% being below AMS measurement uncertainty. SHT samples (IDs TVXX) were processed at the Vienna Laboratory and were measured at VERA and PRIME, respectively. Standards used at PRIME lab were characterized by Nishiizumi et al. (2007). Standards at VERA are secondary standards. For Aluminum, two standards were used: AW-V-2 with a $^{26}Al/^{27}Al$ ratio of 2.71 ± 0.02^{-12} and AW-V-3 with a ratio of 3.55 ± 0.05^{-12}. TVXX 4 was separated into two fractions depending on grain size (1.00–0.50 μm and 0.50–0.25 μm). Al concentrations of double measurements were averaged for burial age calculations.

Site	Sample ID	TCN LAB/AMS	Quartz [g]	^{27}Al total [mg]	$^{26}Al/^{27}Al$ [−]	Error ratio AMS [%]	ICP-OES Error*) [%]	^{26}Al [atoms/g qtz]	Total error ^{26}Al [%]
GDT	GXX-II-1	LDEO/LLNL	24.9272	1.6652	1.453E-13	4.94	0.96	216637	7.73
	GXX-II-2	LDEO/LLNL	25.2633	1.6998	2.010E-13	4.41	0.92	301887	7.40
	GXX-II-3 (1)	LDEO/LLNL	25.3911	3.6422	7.881E-14	9.85	1.21	252318	11.53
	GXX-II-3 (2)	LDEO/LLNL	25.3911	3.6422	7.493E-14	11.28	1.21	239907	12.77
	GXX-II-5	LDEO/LLNL	25.3505	1.7362	1.529E-13	4.86	1.87	233800	7.85
	GXX-II-10	LDEO/LLNL	24.7806	1.6888	5.240E-13	2.52	2.39	797030	6.82
	GXX-III-1	LDEO/LLNL	24.3382	2.1737	1.525E-13	6.13	2.36	303939	8.81
	GXX-III-2	LDEO/LLNL	25.0836	1.7097	2.467E-13	4.04	1.49	375261	7.28
	GXX-III-3	LDEO/LLNL	24.8726	1.6296	1.428E-13	6.17	1.87	208788	8.72
	GXX-III-4	LDEO/LLNL	25.0268	1.6843	1.484E-13	6.04	2.20	222892	8.71
	GXX-III-5	LDEO/LLNL	25.2166	1.7060	1.740E-13	4.86	1.63	262723	7.79
SHT	TVXX 1	VL/VERA	44.1634	0.8369	6.034E-13	11.41	2.66	255231	12.83
	TVXX 2	VL/VERA	40.5659	1.6372	1.534E-13	14.37	1.99	138187	15.52
	TVXX 4 (1.00-0.50)	VL/PRIME	32.0867	2.3207	2.924E-13	5.76	0.70	472096	8.22
	TVXX 4 (0.50-0.25)	VL/PRIME	52.4899	2.6327	4.403E-13	4.70	0.81	492899	7.52
	TVXX 5	VL/PRIME	32.7028	14.7095	1.912E-14	15.20	0.62	191961	16.30
	TVXX 6	VL/PRIME	54.0745	0.8794	2.467E-13	4.04	0.02	89533	7.12

$t_{1/2,Al}$ 705000 ± 24000 yrs (Nishiizumi, 2004).
*) Maximum value combined error of aliquot A, B and C.
Error propagation. $Err_{total,Al} = \sqrt{err^2_{P_{26}} + err^2_{t_{1/2,26}} + err^2_{ratio} + err^2_{ICP-OES}}$.

Table 4
$^{26}Al/^{10}Be$ ratios of GDT and SHT samples. Multiple GDT samples (ID GXX) show elevated ratios (>6.75). ^{10}Be depletion for each affected sample was calculated in order to give a reference for the number of atoms necessary to consolidate ratios (<6.75). TVXX 4 (av.) are the averaged Al and Be values from Tables 2 and 3. Sample ratios plotted in bold font ($^{26}Al/^{10}Be < 6.75$ within errors) were accepted for age calculations.

Site	Sample ID	Quartz [g]	^{10}Be [atoms/g qtz]	^{26}Al [atoms/g qtz]	$^{26}Al/^{10}Be$ [−]	Error $^{26}Al/^{10}Be$ [−]	Error $^{26}Al/^{10}Be$ [%]	^{10}Be Depletion [atoms/g qtz]
GDT	GXX-II-1 (1)	24.9980	26298	216637	8.238	0.821	9.96	5797
	GXX-II-1 (2)	24.9272	26906	–	8.052	0.764	9.48	5188
	GXX-II-2	25.2633	43428	301887	6.951	0.634	9.12	1296
	GXX-II-3 (1)	25.3911	29352	252318	8.596	1.103	12.83	8029
	GXX-II-3 (2)	–	–	239907	8.173	1.141	13.96	6190
	GXX-II-5	25.3505	29821	233800	7.840	0.752	9.59	4816
	GXX-II-10	24.7806	159934	797030	4.983	0.431	8.65	–
	GXX-III-1	24.3382	44038	303939	**6.902**	0.711	10.30	989
	GXX-III-2	25.0836	57443	375261	**6.533**	0.592	9.06	–
	GXX-III-3	24.8726	31015	208788	**6.732**	0.694	10.31	–
	GXX-III-4	25.0268	28365	222892	7.858	0.807	10.27	4656
	GXX-III-5	25.2166	45400	262723	**5.787**	0.548	9.47	–
SHT	TVXX 1	44.1634	43103	255231	**5.921**	0.921	15.55	–
	TVXX 2	40.5659	30901	138187	**4.472**	0.763	17.07	–
	TVXX 4 (av.)	–	88651	482497	**5.443**	0.590	10.85	–
	TVXX 5	32.7028	29107	191961	**6.595**	1.198	18.17	–
	TVXX 6	54.0745	45138	89533	1.984	0.201	10.12	–

Error propagation. $Err_{total} = \sqrt{err^2_{10Be} + err^2_{26Al}}$.

6.75 due to muon production. Muons travel deep into the rock and continue to build up nuclides at depths, where spallogenic production has ceased. Muon production is assumed to establish higher $^{26}Al/^{10}Be$ ratios in rocks at ranges around 7.0 ± 0.4 (negative muon capture) to 7.7 ± 1.4 (fast muon capture) at the surface (Heisinger et al., 2002) and ca. 8.3 to 8.4 in depths of about 10 m depending on rock density (Braucher et al., 2013; Akçar et al., 2017). Samples associated with fast eroding surfaces in the source area are dominated by muon production as rock layers are brought to the surface rapidly. Consequently, $^{26}Al/^{10}Be$ ratio in samples of this type are likely to show $^{26}Al/^{10}Be$ ratios higher than 6.75. Burial ages derived from samples originating from glacial areas need to be calculated using an increased initial nuclide ratio, which captures the pace of erosion in the source area and the muon signal recorded in the samples. The determination of an initial nuclide ratio in cobbles from glacial source areas is challenging and adequate values appear to lie somewhere in the spectrum between 6.75 and 8.4. As this problem is subject of current research, all samples with nuclide ratios above the surface production ratio and without measurement uncertainties falling below 6.75 were eliminated from age calculations, namely GXX-II-1, GXX-II-3, GXX-II-5, GXX-III-4.

GXX-II-10 exhibited significantly higher nuclide concentrations and plotted isolated in an entirely different region of the isochron diagram (Fig. 6a). The sample did not follow a linear relationship reflected by the amalgamated sample, making a strong argument for GXX-II-10 being a reworked clast, which experienced a complex burial history (Balco and Rovey, 2008; Dunai, 2010). Samples, which violate a linear trend provided by the majority of samples, are assumed to be outliers (Balco and Rovey, 2008). The rejection of

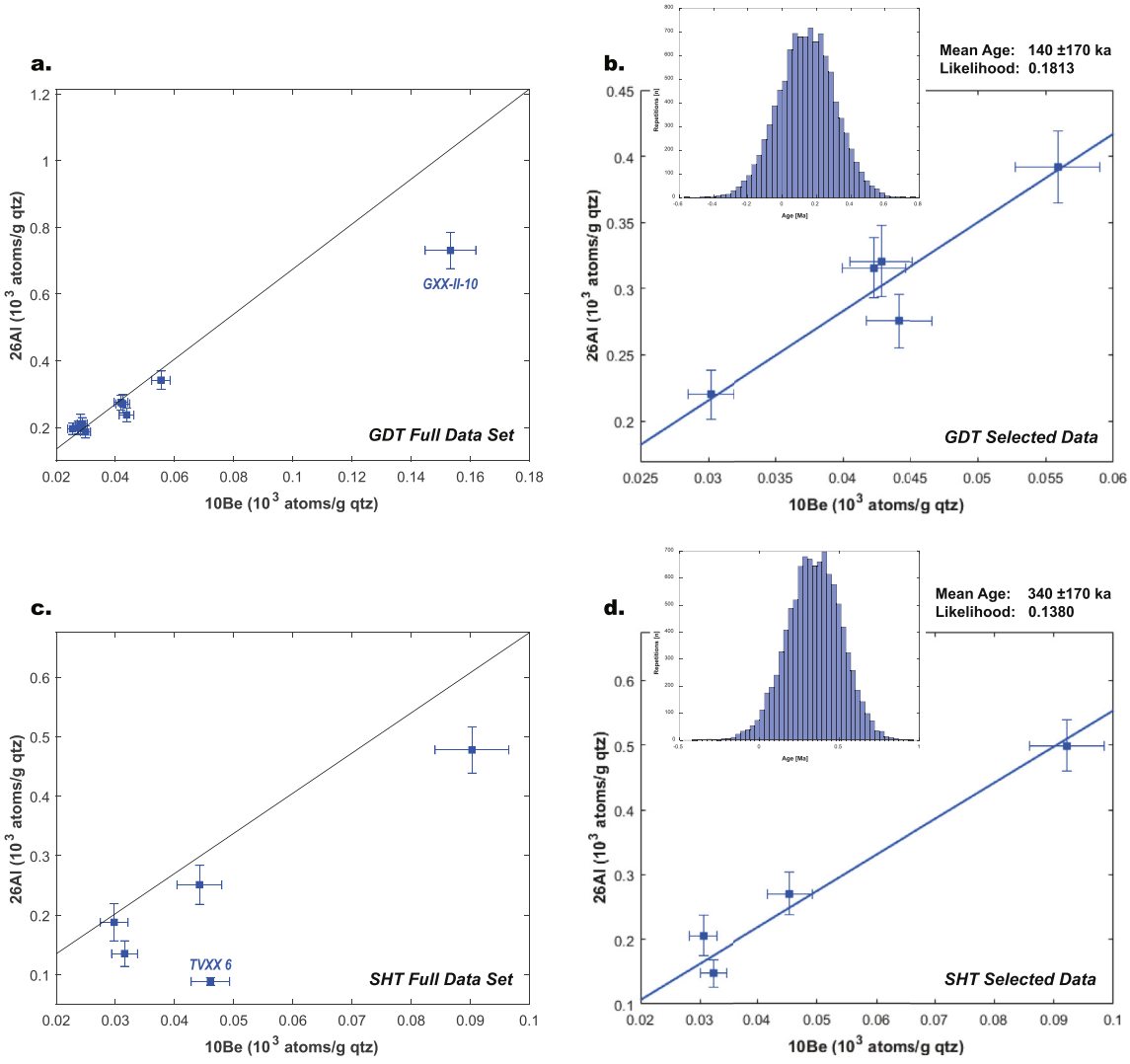

Fig. 6. Isochron plots displaying full GDT and SHT data sets (left column), and selected data sets used for age calculation (right column) for comparison. Black line indicates the surface production ratio of 6.75, colored line indicates the computed isochron. Histogram insets are the results of a Monte-Carlo simulation based on a recursive fit to ^{26}Al and ^{10}Be data to generate an isochron age. The simulation was carried out with 10,000 reruns by varying ^{26}Al/^{10}Be ratios within the measured errors bars. The given ages are the respective mean ages and 1σ standard deviations derived from corresponding histograms.

GXX-II-10 was confirmed by the application of Peirce's criterion, a statistical approach to identify outliers (Peirce, 1852; Gould, 1855; Ross, 2003). Samples GXX-II-2, GXX-III-1, GXX-III-2, GXX-III-3 and GXX-III-5 were accepted for burial age calculations. The isochron, which was calculated based on blank corrected ^{26}Al and ^{10}Be concentrations of accepted GDT samples, produces a mean burial age of 140 ± 170 ka with a likelihood of 0.1813 (Fig. 6b).

At the SHT setting, all samples showed ratios below 6.75. However, one sample with a very low isotope ratio (TVXX 6) was identified as an outlier by applying Peirce's criterion, and was excluded from age calculation (Fig. 6c). TVXX 4 was processed and analyzed twice, one grain size fraction ranging from 1.00 to 0.50 mm and a second one from 0.50 to 0.25 mm. ^{26}Al and ^{10}Be concentrations were averaged and the mean value was used for the burial age calculation, resulting in a burial age of 340 ± 170 ka with a likelihood of 0.1380 (Fig. 6d).

4.2. pIRIR225 ages

The results of gamma spectrometry measurements for the pIRIR225 luminescence samples and the doserate calculations are summarized in Table 5. All samples showed very similar characteristics, with respect to signal intensities and shape of the dose response curves (Fig. 7). For the majority of samples from the SHT site, all measured equivalent doses plot above, or in the upper linear part of the dose response curve though, indicating saturation of the pIRIR225 signal. To properly check for saturation, an additional rejection criterion was applied to the pIRIR225 measurements. The $2D_0$ value marks the point of 86% saturation and was introduced as a criterion for the evaluation of the saturation level of a dose response curve by Murray and Wintle (2003). The IR50 signals taken from the pIRIR225 sequence were not included in further analysis, because the stronger effects of fading present in this signal prevents reliable evaluation of the saturation level. Aliquots were rejected whenever their pIRIR225 equivalent dose was larger (no overlap within errors on the 1σ level) than the individual $2D_0$ value constructed for each dose response curve. For the majority of the SHT samples, all aliquots had to be rejected based on this criterion. However, using the average $2D_0$ value of all aliquots measured for each sample, minimum ages could be calculated for

Table 5
Results from radionuclide analysis and dose rate calculation of pIRIR225 luminescence samples.

Site	Sample ID Lab	Sample ID Field	Depth [m]	^{238}U [ppm]	^{232}Th [ppm]	K [%]	Water content [a] [%]	Cosmic Doserate [Gy/ka]	Doserate Fs [b] (external + internal) [Gy/ka]
GDT	VLL-0199-L	MAR-01	3.7	0.60 ± 0.02	1.98 ± 0.07	1.05 ± 0.02	15 ± 5	0.13 ± 0.01	1.91 ± 0.10
	VLL-0200-L	MAR-02	4	0.45 ± 0.01	1.72 ± 0.07	1.24 ± 0.03	15 ± 5	0.13 ± 0.01	2.01 ± 0.11
	VLL-0201-L	MAR-03	1.2	0.66 ± 0.02	2.23 ± 0.09	1.10 ± 0.02	15 ± 5	0.18 ± 0.02	1.98 ± 0.10
	VLL-0210-L	MAR-04	1	1.33 ± 0.03	5.76 ± 0.20	0.93 ± 0.02	15 ± 5	0.19 ± 0.02	2.20 ± 0.12
SHT	VLL-0222-L	SH-01	3.8	1.21 ± 0.03	4.39 ± 0.16	0.68 ± 0.02	15 ± 5	0.13 ± 0.01	1.89 ± 0.10
	VLL-0223-L	SH-02	0.6	0.89 ± 0.02	4.10 ± 0.15	1.13 ± 0.02	15 ± 5	0.19 ± 0.02	2.25 ± 0.12
	VLL-0224-L	SH-03	1.3	0.49 ± 0.02	1.77 ± 0.08	1.07 ± 0.02	15 ± 5	0.18 ± 0.02	1.89 ± 0.10
	VLL-0232-L	SH-04	7.7	0.54 ± 0.02	1.97 ± 0.08	0.90 ± 0.02	15 ± 5	0.08 ± 0.01	1.77 ± 0.09
	VLL-0233-L	SH-05	6.4	1.16 ± 0.03	4.17 ± 0.16	1.37 ± 0.03	15 ± 5	0.10 ± 0.01	2.42 ± 0.13
	VLL-0234-L	SH-06	1.4	1.20 ± 0.03	4.52 ± 0.17	0.91 ± 0.02	15 ± 5	0.18 ± 0.02	2.09 ± 0.11

[a] Estimated average water content throughout burial time. Values covering rather dry to almost saturated conditions.
[b] Including an alpha attenuation factor of 0.08 ± 0.01 and an internal K content of 12.5 ± 0.5%.

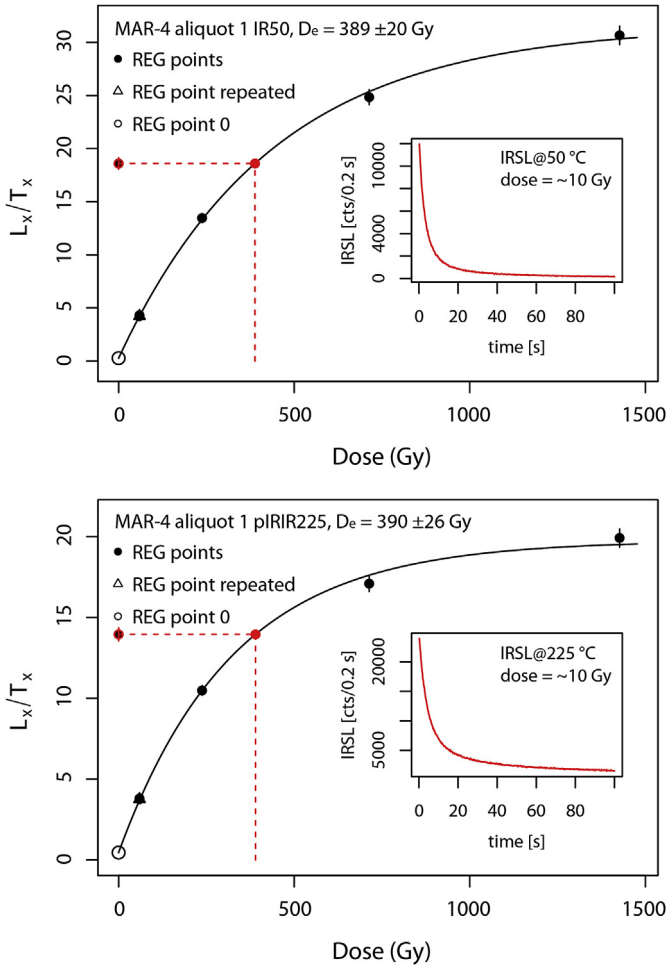

Fig. 7. Representative dose response curves and shinedown curves of an aliquot of sample MAR-04 for both luminescence signals analyzed in this study: IR50 (top) and pIRIR225 (bottom).

these samples (as discussed in Lüthgens et al., 2017). Despite the relatively similar $2D_0$ values for all samples, the calculated minimum ages range from about 190 ka to about 270 ka, depending on the overall doserate for each sample. Only two samples, the stratigraphically youngest sample from each sampling site, show equivalent doses very clearly below saturation level (SH-06 and MAR-04), yielding ages of 34 ± 3 ka (SH-06) and 120 ± 10 ka (MAR-04), respectively. For the three remaining samples from the GDT site (MAR-01, MAR-02, and MAR-03), the large majority of equivalent dose values passes the $2D_0$ rejection criterion, although most equivalent doses overlap within error with the individual $2D_0$ value calculated for each dose response curve. This may likely indicate that these samples are close to saturation, however, an average equivalent dose, and consequently a depositional age, can still be calculated for these samples (Table 6).

5. Discussion

5.1. Methodological considerations on isochron ages

Although half of the cosmogenic GDT sample set was eliminated in the course of data evaluation, predominantly due to ^{26}Al/^{10}Be ratios exceeding the surface production ratio of 6.75, it was possible to calculate a burial age based on the five remaining data points. The resulting isochron age is within errors in agreement with pIRIR225 luminescence ages from the same outcrop. Particularly MAR-01 and MAR-02 collected from positions next to the amalgamated cosmogenic nuclide sample, provide an excellent opportunity for an independent cross-check and underpin the robustness of the GDT data set, even though the mean isochron age lies somewhat below the neighboring pIRIR225 ages. pIRIR225 luminescence and burial ages are coherent within uncertainties.

Often, when measured nuclide concentrations lead to increased ^{26}Al/^{10}Be ratios, the quality of sample preparation and AMS measurements is doubted. Regarding the GDT data set, the probability of laboratory and measurement errors is very small due to double measurements:

- Aliquots of sample GXX-II-1 were processed with two separate sample batches and were analyzed in the course of two independent AMS Beryllium runs. ^{10}Be/^{9}Be ratios of GXX-II-1 (1) and GXX-II-1 (2) correspond to sample fractions that were processed and analyzed independently, yet ratios differ only by 2.29%, being below measurement uncertainties of individual sample ratios, hence demonstrating that the AMS Beryllium data is reproducible and consistent (Table 2).
- Aluminum in GXX-II-3 was relatively high due to a high native Aluminum content, which could not be lowered through extensive purification treatment. The sample was divided and loaded into two separate AMS cathodes. Ratios deviate by 5.04%, a value which is within a normal range of Aluminum isotope analysis (Hunt et al., 2008, Table 3).

In order to extend the testing for procedural and analytical problems, which might be a reason for irregular ^{26}Al/^{10}Be ratios, we evaluated several scenarios that have the potential to cause an

Table 6
Summary of OSL data.

Site	Sample ID Lab	Sample ID Field	Grain Size [μm]	Fs pIRIR225 [a] [n]	Fs pIRIR225 D_e [b] [Gy]	Fs pIRIR225 $2D_0$ [c] [Gy]	Dose Rate Fs [d] [Gy/ka]	Fs pIRIR225 Age [e] [ka]
GDT	VLL-0199-L	MAR-01	200-250	16	517 ± 49	588 ± 60	2.04 ± 0.11	220 ± 20
	VLL-0200-L	MAR-02	200–250	9	559 ± 60	549 ± 52	2.14 ± 0.12	260 ± 30
	VLL-0201-L	MAR-03	200–250	20	485 ± 48	527 ± 43	2.16 ± 0.12	220 ± 30
	VLL-0210-L	MAR-04	200–250	24	296 ± 22	476 ± 24	2.39 ± 0.14	120 ± 10
SHT	VLL-0222-L	SH-01	200–250	5	n/a	529 ± 33	2.02 ± 0.23	>260 ± 20
	VLL-0223-L	SH-02	200–300	4	n/a	512 ± 27	2.44 ± 0.14	>210 ± 20
	VLL-0224-L	SH-03	200–250	5	n/a	530 ± 38	2.07 ± 0.12	>260 ± 20
	VLL-0232-L	SH-04	200–250	4	n/a	506 ± 10	1.85 ± 0.10	>270 ± 20
	VLL-0233-L	SH-05	200–250	5	n/a	479 ± 17	2.52 ± 0.14	>190 ± 10
	VLL-0234-L	SH-06	200–250	28	78 ± 5	449 ± 35	2.27 ± 0.13	34 ± 3

[a] Number of grains passing all rejection criteria.
[b] Error weighted mean ± error weighted standard deviation.
[c] Arithmetic mean ± standard deviation.
[d] Overall doserate. Details please see Table 5.
[e] Ages calculated using the software ADELE (Kulig, 2005) and rounded to tens of thousands of years.

upwards shift of $^{26}Al/^{10}Be$ ratios: (1) neglected native ^{9}Be, (2) loss of ^{10}Be during sample processing, (3) uncertainties in ICP-OES analysis of ^{27}Al and (4) contamination with ^{26}Al.

(1) Native ^{9}Be: The calculation of ^{10}Be relies on the premise that the added Beryllium carrier is the only source of ^{9}Be in the sample. If native Beryllium is present in quartz at a significant level, it adds an unknown amount of ^{9}Be atoms to the nuclide inventory. Unquantified native ^{9}Be leads to an underestimation of ^{10}Be and results in elevated $^{26}Al/^{10}Be$ ratios. In the course of elemental analysis prior to quartz digestion, small amounts of Beryllium were found in three samples (GXX-II-2, GXX-III-1, GXX-III-4). Table 7 displays native ^{9}Be contents and resulting extra ^{10}Be ranging around several hundreds of atoms per gram quartz ($\Delta^{10}Be$). The number of ^{10}Be atoms necessary to bring ratios down to a value of 6.75 are specified in Table 4. The three affected samples were corrected for native Beryllium, but their $^{26}Al/^{10}Be$ ratios did not drop significantly.

(2) Loss of ^{10}Be: Independent double processing and double AMS measurement of GXX-II-1 make a strong case for the consistency of the ^{10}Be data.

(3) ^{27}Al measurement with ICP-OES (Overestimation of ^{27}Al): Accurate values for ^{27}Al contents in samples are crucial to the calculation of ^{26}Al concentrations. The determination of total Aluminum is therefore one of the most delicate parts of cosmogenic nuclide analysis. ICP-OES Aluminum data for GDT samples are reported in the supplementary data section (S 1 and S 2). We took multiple aliquots from each sample at various stages of sample evaporation, which provided good control over possible Aluminum losses or additions linked to the heating of sample solutions. Aluminum concentrations of aliquots were averaged for each individual sample, leading to a sample-specific mean ^{27}Al value with a maximum uncertainty of 2.39%. Blanks spiked with Aluminum carrier hold another opportunity for quality control of the ICP-OES measurement. As the amount of carrier added to the sample is known (analog to ^{9}Be carrier addition), the measured Aluminum content should be in good agreement with the expected content. Deviations between expected and measured contents of two blanks amount to 0.95% and 0.06% promoting confidence in the data set.

(4) Contamination with ^{26}Al: Additions of meteoric ^{26}Al are unlikely as the isotope's production in the atmosphere is by three orders smaller compared to the build-up of ^{10}Be due to lacking target elements (Gosse and Phillips, 2001; Granger et al., 2013).

Nuclide ratios deviating from the $^{26}Al/^{10}Be$ surface production ratio of 6.75, are not unusual and have occurred in numerous previous studies, albeit rather isolated (e.g. Hancock et al., 1999; Häuselmann et al., 2007; Erlanger et al., 2012; Hidy et al., 2014; Davis et al., 2014; Granger et al., 2015; Çiner et al., 2015; McPhillips et al., 2016). Irregularities in these works were mainly attributed to issues concerning laboratory procedures or AMS measurements. Some other recent studies, however, found $^{26}Al/^{10}Be$ ratios systematically deviating from expected values, causing doubt regarding the validity of both, the upper limits of atmospheric and in situ production ratios in terrestrial rock. Auer et al. (2009) determined $^{26}Al/^{10}Be$ ratios in deep Antarctic ice. Nuclide ratios in ice cores are expected to correspond to either the atmospheric production ratio of 1.89×10^{-3}, or to lower values due to radioactive decay over time. The authors analyzed a cluster of samples originating from more than 2500 m depth, which showed $^{26}Al/^{10}Be$ values being well above the expected production ratio in

Table 7
List of samples with native Beryllium found in the course of elemental analysis. Ratios were calculated with and without consideration of native ^{9}Be in order to test the ratios sensitivity towards changes in ^{9}Be at the given level of cosmogenic nuclide concentrations. Additional ^{10}Be atoms ($\Delta^{10}Be$) due to native ^{9}Be amount to some hundreds of atoms per gram quartz and lower ratios only marginally. For burial age calculations, ^{9}Be corrected ratios of GXX-II-2 and GXX-III-1 were used. GXX-III-4 was discarded for further data evaluation because of its nuclide ratio being well above 6.75.

Sample ID	^{9}Be carrier [mg]	Native ^{9}Be [mg]	^{10}Be w/o native ^{9}Be [atoms/g qtz]	^{10}Be w/native ^{9}Be [atoms/g qtz]	$\Delta^{10}Be_n$ [atoms/g qtz]	$^{26}Al/^{10}Be$ w/o native ^{9}Be [−]	$^{26}Al/^{10}Be$ w/native ^{9}Be [−]
GXX-II-2	0.1782	0.0022	43428	43964	536	6.951	6.867
GXX-III-1	0.1763	0.0016	44038	44438	400	6.902	6.840
GXX-III-4	0.1823	0.0021	28365	28692	327	7.858	7.768

the atmosphere.

With respect to the build-up of ^{26}Al and ^{10}Be in terrestrial rock or soil, a number of production rate studies have reported varying ^{26}Al/^{10}Be surface production ratios in the past. Klein et al. (1986) investigated Libyan desert glass and found an in situ ^{26}Al/^{10}Be production ratio of around 7. Nishiizumi et al. (1989) published a ratio of 6.02 ± 0.44 for glacially polished rocks in the Sierra Nevada, which later was corrected to 6.75 subsequent to ^{10}Be standardization. Kubik et al. (1998) studied a landslide in the Eastern Alps, which was dated independently using the radiocarbon method and dendrochronology. They yielded a surface production ratio of 6.52 ± 0.43. In recent years, along with the implementation of the CRONUS Earth Calculator, the value 6.75 was broadly adopted as ^{26}Al/^{10}Be in situ production ratio (Balco et al., 2008). However, ratios being incoherent with this value are continuing to occur. Goethals et al. (2009) analyzed ^{10}Be, ^{26}Al and ^{21}Ne of Bishop Tuff in Eastern California, calculated a ^{26}Al/^{10}Be spallogenic production ratio of 7.76 ± 0.49. Lifton et al. (2014) measured ^{26}Al and ^{10}Be in paleo shorelines of Lake Bonneville in Utah and yielded a ratio of 6.65 ± 0.77. Corbett et al. (2017) analyzed 24 constantly exposed bedrock and boulder surfaces along the western coastline of Greenland and found a nuclide ratio of 7.3 ± 0.3. A comprehensive study by Borchers et al. (2016), where the authors tested the quality of scaling scheme parameters and developed a new production rate calibration procedure, the resulting ^{26}Al/^{10}Be ratio amounts to 7.28. Argento et al. (2013) reported that geographic location, in particular altitude, is not only influencing nuclide production itself, but also affects the ^{26}Al/^{10}Be ratio, which has been considered as globally constant until then. They developed a new physics-based model, which is able to depict the ratio's dependence on elevation and reported a^{26}Al/^{10}Be production ratio of 7 at sea-level and a value of 6.9 at 3000 m asl. As measured nuclide ratios in buried samples evolve from the surface production ratio, the latter not being well constrained is eminently problematic for burial age dating. How to decipher altitude dependent surface production ratios accurately (e.g. Argento et al., 2015), along with the modeling of muon production in the subsurface (Balco, 2017 and references therein) are two major fields of ongoing research.

Apart from uncertainties in the surface production ratio of ^{26}Al and ^{10}Be, there is also a possible process-based explanation for increased ^{26}Al/^{10}Be ratios at the GDT site. Rapid exhumation of fresh bedrock layers increases the relevance of muons as dominant nuclide production pathway prior to exposure. Braucher et al. (2013) measured a muon dominated production ratio of approximately 8.3 for a depth range of 0–6500 g/cm^2; Akçar et al. (2017) calculated a ^{26}Al/^{10}Be of ca. 8.4 at 10 m depth gradually decreasing towards a value of 6.75 at the surface. When rock layers are abraded rapidly and experience only short exposure times, their nuclide inventory has not reached equilibrium with the surface ratio of 6.75. Samples from glacial areas are likely to record a muon production signal from their source area so that ^{26}Al/^{10}Be ratios well above the surface production ratio of 6.75 are possible. Kuhlemann (2007) estimated erosion rates around 30–180 m/Ma for the Northern Calcareous Alps, which supports this argument. Together with the fact that low nuclide concentrations were found in most GDT samples, there is strong evidence that muon production in the samples' source area is a relevant factor at the GDT setting.

Regarding the SHT setting, four out of five ^{26}Al/^{10}Be isotope values were used for isochron age calculation. One clast was rejected due to its low Aluminum content, which may indicate that this sample was previously buried and thus preserved ^{10}Be. The burial age at the base of the SHT (10 m below the surface) yields 340 ± 170 ka.

5.2. Methodological consideration on pIRIR225 ages

Burial ages determined by luminescence dating techniques must be evaluated with regard to factors potentially resulting in unwanted over- or underestimation of ages. Whenever potassium-rich feldspar is used as a dosimeter for luminescence dating purposes, incomplete bleaching of the luminescence signal before burial, leading to an age overestimation, needs to be discussed. The IR50, and especially the pIRIR225 signal of feldspar is known to bleach much more slowly than the luminescence signal of quartz (e.g. Thiel et al., 2011a). Because of the high dose range, no quartz measurements were conducted in this study, however, the comparison of the two detected feldspar signals may also allow an evaluation of the bleaching properties of the samples, because the pIRIR225 signal is expected to bleach even more slowly than the IR50 signal (e.g. Bickel et al., 2015a, 2015b; Murray et al., 2012). For that comparison, all ages must be corrected for fading. We tested this for all samples not showing field saturation, and for those samples, the fading corrected IR50 and pIRIR225 based ages agree within error, indicating that incomplete bleaching was not a significant factor for the samples under investigation. However, we decided not to include these comparative data in the pIRIR225 summary table for two reasons: Firstly, as already described above, fading correction should not be applied in the higher dose range beyond the lower linear part of the dose response curve. This would clearly be the case for all samples in this study. Secondly, the low fading rates detected for the pIRIR225 signal are usually considered as a negligible fading rate (Thiel et al., 2011b). Therefore, we only present ages for the pIRIR225 signal, which were not corrected for fading (Table 6).

5.3. Stratigraphical considerations

Sediments deposited at SHT and GDT settings mainly originate from Alpine catchments or from the Variscian basement of the Bohemian Massif. It appears that the sediment source of both terraces is largely similar, even though the SHT is closer to the Morava river so that there might be minor contribution from its drainage area. Nuclide concentrations at both sites are relatively low, indicating that the clasts have not been exposed to cosmic radiation over long periods of time. Clasts detached from bedrock by valley erosion experienced fast transport rates due to high hillslope gradients prior to their deposition in the Danube's flood plain. High erosions rates in the source areas in combination with short travelling times in river systems or repeated burial episodes may have left only a relatively short time window for cosmogenic nuclide production, being coherent with low nuclide concentrations found in the samples.

Four out of ten samples at the GDT site exhibit increased ^{26}Al/^{10}Be ratios as opposed to the SHT site, where all sample ratios lie below 6.75. This pattern could either be explained by environmental impacts, which might have affected some GDT samples locally, or by a varying geomorphological processes prior to the sediments' deposition (e.g. sediment supply, erosion rates and transport rates in river systems). Due to elevated nuclide ratios occurring at the GDT site exclusively, GDT sediments are more likely to originate from glacial source areas with high erosion rates compared to SHT sediments.

An evaluation of the terrace ages from a paleo-climate perspective shows that the central isochron age of the GDT falls into MIS 6, while pIRIR225 ages indicate MIS 7. This classification might point towards environmental conditions, which promoted glacial erosion, thereby producing large amounts of glacial debris susceptible to mobilization and subsequent transport to the Vienna Basin. A similar interpretation might be valid for the SHT setting,

whose central isochron age falls into MIS 10 and pIRIR225 data provides minimum ages ranging around MIS 7 and 8. We are aware that correlation with MIS is very challenging, given the uncertainties of the determined ages. These first tentative assumptions therefore need to be backed up in the course of future studies. Further cosmogenic nuclide analysis (accompanied by luminescence dating analysis) targeting GDT and SHT sediments, but collected from different terrace sections, could clarify, whether elevated $^{26}Al/^{10}Be$ ratios are isolated to the sampled GDT outcrop, or if they are characteristic for the entire terrace body, but are systematically absent in SHT sediments. This would strongly support the process-based interpretation of the occurrence of the elevated ratios and may qualify them as a preliminary indicator for predominant glacial erosion in the respective sediment source areas.

6. Conclusions

The evaluation of pIRIR225 luminescence and isochron burial dating ages at the GDT and SHT sites allow the following conclusions:

(1) ^{26}Al and ^{10}Be concentration levels in sediments of both terraces are high enough to carry out cosmogenic nuclide analysis successfully, albeit concentrations ranging at the lower end of the feasible spectrum, at least regarding the GDT.
(2) Although half of the GDT cosmogenic nuclide data set had to be rejected, burial ages and pIRIR225 luminescence ages from the site are in good agreement within errors. The GDT isochron burial age suggests that the terrace was deposited ca. 140 ± 170 ka (1σ error), which is supported by pIRIR225 luminescence ages of samples originating from the same outcrop and ranging between 120 ± 10 ka and 260 ± 30 ka. pIRIR225 luminescence ages of the SHT site provide minimum ages due to saturation, but are coherent with the SHT burial dating result of 340 ± 170 ka.
(3) Based on the novel geochronological information, there is strong evidence that the GDT and the SHT did not form concurrently, but are witnesses of two different episodes of increased sediment input into the Vienna Basin. Fault activity in the study area may have had an impact on the morphology of the GDT-SHT complex, but has clearly not solely caused the difference in elevation between the two terrace bodies.
(4) Several cosmogenic nuclide samples at the GDT site showed $^{26}Al/^{10}Be$ ratios above the surface production ratio and were hence eliminated for isochron burial dating calculations. A number of possible scenarios, which might explain increased $^{26}Al/^{10}Be$ ratios, were evaluated (e.g. chemical procedures, carrier characterization, native Beryllium, ICP-OES), but procedural or analytical errors were shown to be unlikely. Isolated samples with increased ratios together with systematic deviations in recent studies give cause for speculations about the validity of 6.75 as upper limit for $^{26}Al/^{10}Be$ surface production ratios. Especially when it comes to sediment source areas in glacial regions, typically affected by high erosion rates, it is likely that nuclide ratios are dominated by muon production prior to the clasts' exhumation. When the mobilization of clasts is followed by only short periods of exposure to cosmic radiation, and short burial times, it appears that there is not enough time for the ratio to consolidate towards the surface production ratio of 6.75. Values of up to 8.4 have been shown to be more accurate to characterize initial, preburial $^{26}Al/^{10}Be$ ratios in samples originating from glacial areas. Recent studies have broadened our knowledge on isochron age calculations with sediments derived from glacial areas (Braucher et al., 2013; Akçar et al., 2017). However, more research is needed in order to develop a strategy to estimate initial $^{26}Al/^{10}Be$ ratios, especially in sediments where muon production is relevant.

Acknowledgements

The project was funded by the Austrian Science Fund (FWF): P23138-N19. Sandra M. Braumann was supported by the Career Advancement Scholarship (Förderungsstipendium) provided by BOKU. Sandra M. Braumann thanks the LDEO cosmogenic isotope group, in particular the laboratory staff Roseanne Schwartz, Jeremey Frisch and Jean Hanley, as well as Robert C. Finkel for numerous discussions on methodological questions. Stephanie Neuhuber thanks Monika Horschinegg and Wencke Wegner for access to the Geochronolgy facilities at the University of Vienna. The authors are grateful to Eike Rades and Lukas Bickel for field assistance and to Georg Rotomer for proofreading. Finally, the authors graciously thank Naki Akçar and Draženko Nenadić, who reviewed the manuscript and helped to improve it substantially.

Appendix A. Supplementary data

Supplementary data related to this article can be found at https://doi.org/10.1016/j.quaint.2018.01.009.

References

Adamiec, G., Aitken, M., 1998. Dose-rate conversion factors: Update. Ancient TL 16, 37–50.
Akçar, N., Ivy-Ochs, S., Alfimov, V., Schlunegger, F., Claude, A., Reber, R., Christl, M., Vockenhuber, C., Dehnert, A., Rahn, M., Schlüchter, C., 2017. Isochron-burial dating of glaciofluvial deposits: first results from the Swiss Alps. Earth Surf. Process. Landforms 42 (14).
Argento, D.C., Reedy, R.C., Stone, J.O., 2013. Modeling the earth's cosmic radiation. Nucl. Instrum. Methods Phys. Res. Sect. B Beam Interact. Mater. Atoms 294, 464–469.
Argento, D.C., Stone, J.O., Reedy, R.C., O'Brien, K., 2015. Physics-based modeling of cosmogenic nuclides part II - key aspects of in-situ cosmogenic nuclide production. Quat. Geochronol. 26 (1), 44–55.
Auclair, M., Lamothe, M., Huot, S., 2003. Measurement of anomalous fading for feldspar IRSL using SAR. Radiat. Meas. 37, 487–492.
Auer, M., Wagenbach, D., Wild, E.M., Wallner, A., Priller, A., Miller, H., Kutschera, W., 2009. Cosmogenic ^{26}Al in the atmosphere and the prospect of a $^{26}Al/^{10}Be$ chronometer to date old ice. Earth Planet Sci. Lett. 287 (3–4), 453–462.
Balco, G., 2017. Production rate calculations for cosmic-ray-muon produced ^{10}Be and ^{26}Al benchmarked against geological calibration data. Quat. Geochronol. 39, 150–173.
Balco, G., Rovey, C.W., 2008. An isochron method for cosmogenic-nuclide dating of buried soils and sediments. Am. J. Sci. 308 (10), 1083–1114.
Balco, G., Soreghan, G.S., Sweet, D.E., Marra, K.R., Bierman, P.R., 2013. Cosmogenic-nuclide burial ages for Pleistocene sedimentary fill in Unaweep Canyon, Colorado. USA Quat. Geochronol. 18, 149–157.
Balco, G., Stone, J.O., Lifton, N.A., Dunai, T.J., 2008. A complete and easily accessible means of calculating surface exposure ages or erosion rates from ^{10}Be and ^{26}Al measurements. Quat. Geochronol. 3 (3), 174–195.
Beidinger, A., Decker, K., 2011. 3D geometry and kinematics of the Lassee flower structure: implications for segmentation and seismotectonics of the Vienna Basin strike-slip fault, Austria. Tectonophysics 499 (1–4), 22–40.
Beidinger, A., Decker, K., 2014. Quantifying early miocene in-sequence and out-of-sequence thrusting at the alpine-carpathian junction. Tectonics 33, 222–252.
Bender, A.M., Amos, C.B., Bierman, P., Rood, D.H., Staisch, L., Kelsey, H., Sherrod, B., 2016. Differential uplift and incision of the Yakima River terraces, central Washington State. J. Geophys. Res. Solid Earth 121 (1), 365–384.
Bickel, L., Lüthgens, C., Lomax, J., Fiebig, M., 2015a. Luminescence dating of glaciofluvial deposits linked to the penultimate glaciation in the Eastern Alps. Quat. Int. 357, 110–124.
Bickel, L., Lüthgens, C., Lomax, J., Fiebig, M., 2015b. The timing of the penultimate glaciation in the northern Alpine Foreland: new insights from luminescence dating. Proc. Geologists' Assoc. 126, 536–550.
Borchers, B., Marrero, S., Balco, G., Caffee, M., Goehring, B., Lifton, N., Stone, J., 2016. Geological calibration of spallation production rates in the CRONUS-Earth project. Quat. Geochronol. 31, 188–198.
Bøtter-Jensen, L., Andersen, C., Duller, G., Murray, A., 2003. Developments in radiation, stimulation and observation facilities in luminescence measurements.

Radiat. Meas. 37, 535–541.
Bøtter-Jensen, L., Bulur, E., Duller, G., Murray, A., 2000. Advances in luminescence instrument systems. Radiat. Meas. 32, 523–528.
Braucher, R., Bourlès, D., Merchel, S., Vidal Romani, J., Fernadez-Mosquera, D., Marti, K., Keddadouche, K., 2013. Determination of muon attenuation lengths in depth profiles from in situ produced cosmogenic nuclides. Nucl. Instrum. Methods Phys. Res. Sect. B Beam Interact. Mater. Atoms 294, 484–490.
Braucher, R., Brown, E.T., Bourlès, D.L., Colin, F., 2003. In situ produced ^{10}Be measurements at great depths: implications for production rates by fast muons. Earth Planet Sci. Lett. 211 (3–4), 251–258.
Brown, E.T., Brook, E.J., Raisbeck, G.M., Yiou, F., Kurz, M.D., 1992. Effective attenuation lengths of cosmic rays producing ^{10}Be and ^{26}Al in quartz: implications for exposure age dating. Geophys. Res. Lett. 19 (4), 369–372.
Brown, E.T., Bourlès, D.L., Colin, F., Raisbeck, G.M., Yiou, F., Desgarceaux, S., 1995. Evidence for muon-induced production of ^{10}Be in near-surface rocks from Congo. Geophys. Res. Lett. 22 (6), 702–706.
Buylaert, J., Jain, M., Murray, A., Thomsen, K., Thiel, C., Sohbati, R., 2012. A robust feldspar luminescence dating method for Middle and Late Pleistocene sediments. Boreas 41, 435–451.
Buylaert, J., Murray, A., Thomsen, K., Jain, M., 2009. Testing the potential of an elevated temperature IRSL signal from K-feldspar. Radiat. Meas. 44, 560–565.
Chmeleff, J., von Blanckenburg, F., Kossert, K., Jakob, D., 2010. Determination of the Be-10 half-life by multicollector ICP-MS and liquid scintillation counting. Nucl. Instrum. Methods Phys. Res. Sect. B Beam Interact. Mater. Atoms. 268 (2), 192–199.
Çiner, A., Doğan, U., Yıldırım, C., Akçar, N., Ivy-Ochs, S., Alfimov, V., Schlüchter, C., 2015. Quaternary uplift rates of the Central Anatolian Plateau, Turkey: insights from cosmogenic isochron-burial nuclide dating of the Kızılırmak River terraces. Quat. Sci. Rev. 107, 81–97.
Corbett, L.B., Bierman, P.R., Rood, D.H., Caffee, M.W., Lifton, N.A., Woodruff, T.E., 2017. Cosmogenic ^{26}Al/^{10}Be surface production ratio in Greenland. Geophys. Res. Lett. 44 (3), 1350–1359.
Davis, M., Matmon, A., Placzek, C.J., McIntosh, W., Rood, D.H., Quade, J., 2014. Cosmogenic nuclides in buried sediments from the hyperarid Atacama Desert, Chile. Quat. Geochronol. 19, 117–126.
Decker, K., 1996. Miocene tectonics at the alpine-carpathian junction and the evolution of the Vienna Basin. Mitteilungen der Gesellschaft der Geologie- und Bergbaustudenten in Österreich 41, 33–44.
Decker, K., Peresson, H., Hinsch, R., 2005. Active tectonics and quaternary basin formation along the Vienna Basin Transform Fault. Quat. Sci. Rev. 24 (3–4), 307–322.
Dunai, T.J., 2010. Cosmogenic Nuclides: Principles, Concepts and Applications in the Earth Surface Sciences. Cambridge University Press, Cambridge.
Eppensteiner, H., van Husen, D., Krzemien, R., 1973. Beobachtungen an pleistozänen Driftblöcken des Moravafeldes. Wien: Verh. Geol. B.-A 2, 331–336.
Erlanger, E.D., Granger, D.E., Gibbon, R.J., 2012. Rock uplift rates in South Africa from isochron burial dating of fluvial and marine terraces. Geology 40 (11), 1019–1022.
Fink, J., 1977. Jüngste Schotterakkumulation im österreichischen Donauabschnitt. Erdwiss. Forsch. 13, 191–211.
Fink, J., 1981. Die Entwicklung der Landschaft. In: Museen der Stadt Wien (Ed.), Aspern – Von der Steinzeit zum Motorenwerk. Eigenverlag der Museen der Stadt Wien, Wien.
Fink, J., Majdan, H., 1954. Zur Gliederung der pleistozänen Terrassen des Wiener Raumes. Wien: Jb. Geol. B.-A 97, 211–249.
Fuchs, W., Grill, R., 1984. Geologische Karte von Wien und Umgebung - 1:200.000. Geologische Bundesanstalt Österreich, Wien.
Goethals, M.M., Hetzel, R., Niedermann, S., Wittmann, H., Fenton, C.R., Kubik, P.W., von Blanckenburg, F., 2009. An improved experimental determination of cosmogenic ^{10}Be/^{21}Ne and ^{26}Al/^{21}Ne production ratios in quartz. Earth Planet Sci. Lett. 284 (1–2), 187–198.
Gosse, J.C., Phillips, F.M., 2001. Terrestrial in situ cosmogenic nuclides: theory and application. Quat. Sci. Rev. 20, 1475–1560.
Gould, B.A., 1855. On Peirce's criterion for the rejection of doubtful observations, with tables for facilitating its application. Astron. J. 4, 81–87.
Granger, D.E., 2006. A review of burial dating methods using ^{26}Al and ^{10}Be. Geological Society of America Special Papers 415, 1–16.
Granger, D.E., 2014. Cosmogenic nuclide burial dating in archaeology and paleoanthropology. In: Holland, H.D., Turekian, K.K. (Eds.), Treatise on Geochemistry, second ed., vol. 14. Elsevier, Oxford, pp. 81–97.
Granger, D.E., Gibbon, R.J., Kuman, K., Clarke, R.J., Bruxelles, L., Caffee, M.W., 2015. New cosmogenic burial ages for sterkfontein member 2 australopithecus and member 5 oldowan. Nature 522 (7554), 85–88.
Granger, D.E., Lifton, N.A., Willenbring, J.K., 2013. A cosmic trip: 25 years of cosmogenic nuclides in geology. Bull. Geol. Soc. Am. 125 (9–10), 1379–1402.
Granger, D.E., Muzikar, P.F., 2001. Dating sediment burial with in situ-produced cosmogenic nuclides: theory, techniques, and limitations. Earth Planet Sci. Lett. 188 (1–2), 269–281.
Hancock, G.S., Anderson, R.S., Chadwick, O.A., Finkel, R.C., 1999. Dating fluvial terraces with ^{10}Be and ^{26}Al profiles: application to the wind river, Wyoming. Geomorphology 27 (1–2), 41–60.
Häuselmann, P., Fiebig, M., Kubik, P.W., Adrian, H., 2007. A first attempt to date the original "Deckenschotter" of Penck and Brückner with cosmogenic nuclides. Quat. Int. 164–165, 33–42.
Heisinger, B., Lal, D., Jull, A.J.T., Kubik, P., Ivy-Ochs, S., Neumaier, S., Nolte, E., 2002. Production of selected cosmogenic radionuclides by muons: 1. Fast muons. Earth Planet Sci. Lett. 200 (3), 345–355.
Hidy, A.J., Gosse, J.C., Blum, M.D., Gibling, M.R., 2014. Glacial-interglacial variation in denudation rates from interior Texas, USA, established with cosmogenic nuclides. Earth Planet Sci. Lett. 390, 209–221.
Hinsch, R., Decker, K., 2011. Seismic slip rates, potential subsurface rupture areas and seismic potential of the Vienna Basin Transfer Fault. Int. J. Earth Sci. 100 (8), 1925–1935.
Hinsch, R., Decker, K., Wagreich, M., 2005. 3-D mapping of segmented active faults in the southern Vienna Basin. Quat. Sci. Rev. 24 (3–4), 321–336.
Hölzel, M., Decker, K., Zámolyi, A., Strauss, P., Wagreich, M., 2010. Lower miocene structural evolution of the central Vienna Basin (Austria). Mar. Petrol. Geol. 27 (3), 666–681.
Hunt, A.L., Larsen, J., Bierman, P.R., Petrucci, G.A., 2008. Investigation of factors that affect the sensitivity of accelerator mass spectrometry for cosmogenic Be-10 and Al-26 isotope analysis. Anal. Chem. 80 (5), 1656–1663.
Huntley, D., Baril, M., 1997. The K content of the K-feldspars being measured in optical and thermoluminescence dating. Ancient TL 15, 11–13.
Huntley, D., Lamothe, M., 2001. Ubiquity of anomalous fading in K-feldspars and the measurement and correction for it in optical dating. Can. J. Earth Sci. 38, 1093–1106.
Klein, J., Giegengack, R., Middleton, R., Sharma, P.T., Underwood, J.R., Weeks, R.A., 1986. Revealing histories of exposure using in situ produced ^{26}Al and ^{10}Be in Libyan desert glass. Radiocarbon 28 (2A), 547–555.
Korschinek, G., Bergmaier, A., Faestermann, T., Gerstmann, U.C., Knie, K., Rugel, G., Kossert, K., 2010. A new value for the half-life of ^{10}Be by heavy-ion elastic recoil detection and liquid scintillation counting. Nucl. Instrum. Methods Phys. Res. Sect. B Beam Interact. Mater. Atoms 268 (2), 187–191.
Kováč, M., Baráth, I., Harzhauser, M., Hlavatý, I., Hudáčková, N., 2004. Miocene depositional systems and sequence stratigraphy of the Vienna Basin. CFS Courier Forschungsinstitut Senckenberg 246, 187–212.
Krbetschek, M., Götze, J., Dietrich, A., Trautmann, T., 1997. Spectral information from minerals relevant for luminescence dating. Radiat. Meas. 27 (5/6), 695–748.
Kubik, P.W., Ivy-Ochs, S., Masarik, J., Frank, M., Schlüchter, C., 1998. ^{10}Be and ^{26}Al production rates deduced from an instantaneous event within the dendrocalibration curve, the landslide of Köfels, Ötz Valley, Austria. Earth Planet Sci. Lett. 161 (1–4), 231–241.
Kuhlemann, J., 2007. Paleogeographic and paleotopographic evolution of the swiss and eastern Alps since the oligocene. Global Planet. Change 58 (1–4), 224–236.
Kulig, G., 2005. Erstellung einer Auswertesoftware zur Altersbestimmung mittels Lumineszenzverfahren unter spezieller Berücksichtigung des Einflusses radioaktiver Ungleichgewichte in der 238 U-Zerfallsreihe. Technical University Bergakademie Freiberg.
Kullmann, E., 1966. The role of neotectonic movements in the development of ground water reservoirs in the north-eastern part of the Vienna Basin. IAHS Redbook 120, 392–400.
Küpper, H., 1955. Ausblick auf das Pleistozän des Raumes von Wien. Wien: Verh. Geol. B.-A., Sonderheft D 136–152.
Lal, D., 1991. Cosmic ray labeling of erosion surfaces: in situ nuclide production rates and erosion models. Earth Planet Sci. Lett. 104 (2–4), 424–439.
Lal, D., 1988. In situ-produced cosmogenic isotopes in terrestrial rock. Annu. Rev. Earth Planet Sci. 16, 355–388.
Lal, D., Arnold, J.R., 1985. Tracing quartz through the environment. Proc. Indian Acad. Sci. Earth Planet Sci. 94 (1), 1–5.
LDEO, 2009a. Separation and Purification of Quartz from Whole Rock. Retrieved online [14.04.2017]. http://www.ldeo.columbia.edu/sites/default/files/uploaded/image/quartzpuremethod.pdf.
LDEO, 2009b. Extraction of Beryllium from Quartz. Retrieved online [14.04.2017]. http://www.ldeo.columbia.edu/sites/default/files/uploaded/image/bechem-method.pdf.
Lee, E.Y., Wagreich, M., 2016. Polyphase tectonic subsidence evolution of the Vienna Basin inferred from quantitative subsidence analysis of the northern and central parts. Int. J. Earth Sci. 106 (2), 687–705.
Lifton, N., Sato, T., Dunai, T.J., 2014. Scaling in situ cosmogenic nuclide production rates using analytical approximations to atmospheric cosmic-ray fluxes. Earth Planet Sci. Lett. 386, 149–160.
Lüthgens, C., Neuhuber, S., Grupe, S., Payer, T., Peresson, M., Fiebig, M., 2017. Geochronological investigations using a combination of luminescence and cosmogenic nuclide burial dating of drill cores from the Vienna Basin. Z. Dtsch. Ges. Geowiss. 168 (1), 115–140.
Matmon, A., Hidy, A.J., Vainer, S., Crouvi, O., Fink, D., Erel, Y., Horwitz, L.K., Chazan, M., Team, A., 2015. New chronology for the southern Kalahari Group sediments with implications for sediment-cycle dynamics and early hominin occupation. Quat. Res. 84 (1), 118–132.
McPhillips, D., Hoke, G.D., Liu-Zeng, J., Bierman, P.R., Rood, D.H., Niedermann, S., 2016. Dating the incision of the Yangtze River gorge at the First Bend using three-nuclide burial ages. Geophys. Res. Lett. 43 (1), 101–110.
Mejdahl, V., 1979. Thermoluminescence dating: beta attenuation in quartz grains. Archaeometry 21, 61–73.
Murray, A., Thomsen, K., Masuda, N., Buylaert, J., Jain, M., 2012. Identifying well-bleached quartz using the different bleaching rates of quartz and feldspar luminescence signals. Radiat. Meas. 47, 688–695.
Murray, A., Wintle, A., 2003. The single aliquot regenerative dose protocol: potential for improvements in reliability. Radiat. Meas. 37, 377–381.
Nishiizumi, K., 2004. Preparation of Al-26 AMS standards. Nucl. Instrum. Methods

Phys. Res. Sect. B Beam Interact. Mater. Atoms 223, 388–392.
Nishiizumi, K., Imamura, M., Caffee, M.W., Southon, J.R., Finkel, R.C., McAninch, J., 2007. Absolute calibration of Be-10 AMS standards. Nucl. Instrum. Methods Phys. Res. Sect. B Beam Interact. Mater. Atoms 258 (2), 403–413.
Nishiizumi, K., Kohl, C.P., Winterer, E.L., Klein, J., Middleton, R., 1989. Cosmic ray production rates of Be-10 and Al-26 in quartz from glacially polished rocks. Nature 319 (6049), 134–136.
Nishiizumi, K., Lal, D., Klein, J., Middleton, R., Arnold, J.R., 1986. Production of ^{10}Be and ^{26}Al by cosmic rays in terrestrial quartz in situ and implications for erosion rates. J. Geophys. Res. 94 (B12), 17907–17915.
Peirce, B., 1852. Criterion for the rejection of doubtful observations. Astron. J. 2, 161–163.
Penck, A., Brückner, E., 1909. Die Alpen im Eiszeitalter. Tauchnitz, Leipzig.
Peresson, H., Decker, K., 1997. The Tertiary dynamics of the northern Eastern Alps (Austria): changing paleostresses in a collisional plate boundary. Tectonophysics 272, 125–157.
Prescott, J., Hutton, J., 1994. Cosmic ray distributions to dose rates for luminescence and ESR dating: large depths and long-term variations. Radiat. Meas. 23, 497–500.
Prescott, J., Stephan, L., 1982. The contribution of cosmic radiation to the environmental dose for thermoluminescent dating – latitude, altitude and depth dependencies. PACT 6, 17–25.
Preusser, F., Degering, D., Fuchs, M., Hilgers, A., Kadereit, A., Klasen, N., Krbetschek, M., Richter, D., Spencer, J., 2008. Luminescence dating: basics, methods and applications. E&G Quat. Sci. J. 57, 95–149.
Rades, E., Fiebig, M., Lüthgens, C., in press. Luminescence dating of the Rissian type section in southern Germany as a base for correlation. Quat. Int., (in press), corrected proof, https://doi.org/10.1016/j.quaint.2016.07.055.
Rhodes, E., 2011. Optically stimulated luminescence dating of sediments over the past 200,000. Annu. Rev. Earth Planet Sci. 39, 461–488.
Ross, S.M., 2003. Peirce's criterion for the elimination of suspect experimental data. J. Eng. Technol. 20 (2), 38–41.
Royden, L.H., 1985. The Vienna Basin: a thin-skinned pull-apart basin. SEPM Special Publ. 37, 320–338.
Ruszkiczay-Rüdiger, Z., Braucher, R., Novothny, Á., Csillag, G., Fodor, L., Molnár, G., Madarász, B., 2016. Tectonic and climatic control on terrace formation: coupling in situ produced 10Be depth profiles and luminescence approach, Danube River, Hungary. Cent. Eur. Quat. Sci. Rev. 131, 127–147.
Salcher, B., 2008. Sedimentology and Modelling of the Mitterndorf Basin. Dissertation. University of Vienna, Wien, p. 108.
Salcher, B.C., Meurers, B., Smit, J., Decker, K., Hölzel, M., Wagreich, M., 2012. Strike-slip tectonics and Quaternary basin formation along the Vienna Basin fault system inferred from Bouguer gravity derivatives. Tectonics 31 (3), 1–21.
Salcher, B.C., Wagreich, M., 2010. Climate and tectonic controls on Pleistocene sequence development and river evolution in the Southern Vienna Basin (Austria). Quat. Int. 222 (1–2), 154–167.
Salcher, B.C., Frank-Fellner, C., Lomax, J., Preusser, F., Ottner, F., Scholger, R., Wagreich, M., 2017. Middle to Late Pleistocene multi-proxy record of environmental response to climate change from the Vienna Basin, Central Europe (Austria. Quat. Sci. Rev. 173, 193–210. https://doi.org/10.1016/j.quascirev.2017.08.014.
Schaller, M., Ehlers, T.A., Stor, T., Torrent, J., Lobato, L., Christl, M., Vockenhuber, C., 2016. Timing of European fluvial terrace formation and incision rates constrained by cosmogenic nuclide dating. Earth Planet Sci. Lett. 451, 221–231.
Stone, J.O., 2000. Air pressure and cosmogenic isotope production. J. Geophys. Res. 105 (B10), 23753–23759.
Strauss, P., Harzhauser, M., Hinsch, R., Wagreich, M., 2006. Sequence stratigraphy in a classic pull-apart basin (Neogene, Vienna Basin) – a 3D seismic based integrated approach. Geol. Carp 57, 185–197.
Tanasković, L., Stejić, P., Nenadić, D., 2017. Stratigraphic position of the Danube River Terraces in Eastern Serbia. Comptes rendus de l'Académie Bulgare des Sciences (Proceedings of the Bulgarian Academy of Sciences) 70 (5), 671–679.
Thenius, E., 1974. Geologie der Österreichischen Bundesländer in kurz gefassten Einzeldarstellungen - Niederösterreich. Verhandlungen der Geologischen Bundesanstalt. Geologische Bundesanstalt, Wien, p. 273.
Thiel, C., Buylaert, J., Murray, A., Terhorst, B., Hofer, I., Tsukamoto, S., Frechen, M., 2011a. Luminescence dating of the Stratzing loess profile (Austria) – testing the potential of an elevated temperature post-IR IRSL protocol. Quat. Int. 234, 23–31.
Thiel, C., Buylaert, J., Murray, A., Tsukamoto, S., 2011b. On the applicability of post-IR IRSL dating to Japanese loess. Geochronometria 38, 369–378.
Tu, H., Shen, G.J., Granger, D., Yang, X.Y., Lai, Z.P., 2017. Isochron Al-26/Be-10 burial dating of the Lantian hominin site at Gongwangling in Northwestern China. Quat. Geochronol. 41, 174–179.
van Husen, D., Reitner, J., 2011. An outline of the quaternary stratigraphy of Austria. E&G Quat. Sci. J. 60 (2), 366–387.
Weissl, M., Hintersberger, E., Lomax, J., Lüthgens, C., Decker, K., 2017. Active tectonics and geomorphology of the Gaenserndorf terrace in the central Vienna Basin (Austria). Quat. Int. 451, 209–222.
Wessely, G., 2006. Wiener becken. In: Wessely, G. (Ed.), Niederösterreich – Geologie der Österreichischen Bundesländer. Geologische Bundesanstalt, Wien, pp. 189–224.
Wintle, A., 1973. Anomalous fading of thermo-luminescence in mineral samples. Nature 245, 143–144.
Wintle, A., 2008. Luminescence dating: where it has been and where it is going. Boreas 37, 471–482.
York, D., Evensen, N.M., Martinez, M.L., Delgado, J.D., 2004. Unified equations for the slope, intercept, and standard errors of the best straight line. Am. J. Phys. 72 (3), 367–375.
Zhao, Z.J., Granger, D., Zhang, M.H., Kong, X.G., Yang, S.L., Chen, Y., Hu, E.Y., 2016. A test of the isochron burial dating method on fluvial gravels within the Pulu volcanic sequence, West Kunlun Mountains, China. Quat. Geochronol. 34, 75–80.